

Electromagnetic Probes at RHIC-II

G. David¹, R. Rapp² and Z. Xu¹

¹Physics Department, Brookhaven National Laboratory, Upton, NY 11793-5000, USA

²Cyclotron Institute and Physics Department, Texas A&M University, College Station, TX 77843-3366, USA

We summarize how future measurements of electromagnetic (e.m.) probes at the Relativistic Heavy Ion Collider (RHIC), in connection with theoretical analysis, can advance our understanding of strongly interacting matter at high energy densities and temperatures. After a brief survey of the important role that e.m. probes data have played at the Super Proton Synchrotron (SPS, CERN) and RHIC to date, we identify key physics objectives and observables that remain to be addressed to characterize the (strongly interacting) Quark-Gluon Plasma (sQGP) and associated transition properties at RHIC. These include medium modifications of vector mesons via low-mass dileptons, a temperature measurement of the hot phases via continuum radiation, as well as γ - γ correlations to characterize early source sizes. We outline strategies to establish microscopic matter and transition properties such as the number of degrees of freedom in the sQGP, the origin of hadron masses and manifestations of chiral symmetry restoration, which will require accompanying but rather well-defined advances in theory. Increased experimental precision, order of magnitude higher statistics than currently achievable, as well as a detailed scan of colliding species and energies are then mandatory to achieve sufficient discrimination power in theoretical interpretations. This can be achieved with hardware upgrades to the large RHIC detectors (PHENIX, STAR) as well as an increase in luminosity by at least a factor of 10 over the next few years as envisioned in the process leading to RHIC-II.

Contents

1	INTRODUCTION	4
1.1	Toward Discovery and Characterization of Hot and Dense QCD Matter . . .	4
1.2	Where EM Probes Are Unique or Very Important	6
1.3	Theory vs. Experiment at the CERN-SPS	7
2	THEORETICAL CONSIDERATIONS AND PREDICTIONS	9
2.1	Objectives and Framework	9
2.2	QCD Lattice Results	11
2.3	Sum Rules	13
2.3.1	QCD Sum Rules	13
2.3.2	Chiral Sum Rules	13
2.4	Temperature and Degrees of Freedom	16
2.4.1	Suitable Kinematic Regimes	16
2.4.2	Direct Photons and Current RHIC Data	17
2.4.3	Chemical Off-Equilibrium	19
2.4.4	Pre-Equilibrium and Jet-Plasma Emission	20
2.5	In-Medium Spectral Functions below and above T_c	21
2.5.1	Hadronic Many-Body Theory and Chiral Virial Expansion	21
2.5.2	Dropping Mass	23
2.5.3	Resonances in the sQGP	24
2.6	Low-Mass Dilepton Spectra	25
2.7	Chiral Symmetry Restoration	27
2.7.1	Direct and Indirect Approach	27
2.7.2	LMR-IMR Transition: Chiral Mixing	28
2.8	Electromagnetic Signatures of the Color Glass Condensate	30
2.8.1	Dilepton and Photon Production	31
3	OBSERVABLES: STATE OF THE ART	34
3.1	Low-Mass Dileptons	34
3.2	The $\phi(1020)$: Hadronic vs. Leptonic Decays and v_2	35
3.3	Photon Azimuthal Asymmetries (Elliptic Flow)	37
3.4	Electron R_{AA} and Flow	38
3.5	Direct Photons via Low-Mass Dielectrons	38
4	THE FUTURE	40
4.1	Detector upgrades	40
4.1.1	STAR Time-of-Flight and Heavy Flavor Tracker	40
4.1.2	PHENIX Hadron Blind Detector and Silicon Vertex Detector	42
4.1.3	The PHENIX Nose-Cone Calorimeter	43
4.2	New Measurements	44
4.2.1	Direct Photon Correlations (HBT)	44
4.2.2	Spectral Distributions of the a_1 Meson	46
4.3	High Statistics and Energy/Species Scan	47

Electromagnetic Probes at RHIC-II

3

5 SUMMARY AND CONCLUDING REMARKS

49

1. INTRODUCTION

1.1. Toward Discovery and Characterization of Hot and Dense QCD Matter

Among the key goals of ultrarelativistic heavy-ion collisions is the creation of hot and dense strongly interacting matter that (i) resembles the conditions in the early universe, (ii) can be related to the phase diagram of the underlying theory (Quantum Chromodynamics (QCD)), and, (iii) enables the discovery of new phases. Recent surveys of the four experiments at the Relativistic Heavy Ion Collider (RHIC) [1, 2, 3, 4] on results from the first three years of data taking are unanimous in their conclusion that a new form of matter has been created. This matter is very dense, opaque and exhibits a high level of collectivity including evidences at the partonic level. It is inconsistent with naive expectations based on a weakly interacting (gas-like) Quark Gluon Plasma (wQGP), while it is best described in terms of a so-called strongly interacting QGP (sQGP) constituting an almost perfect fluid. Thus, a discovery has been made in a *qualitative* sense, but the properties of this new state of matter remain under intense debate.

A closer look indeed reveals that we are still quite far from a *coherent* and *quantitative* description of the sQGP at RHIC. A first step in this direction is rendered possible by the wealth and precision of new data from Run-4 and Run-5 [5], where measurements of previously inaccessible signals, (e.g., semileptonic electron-decay spectra, J/ψ production or 3-hadron correlations) and improvements on the range, as well as statistical and systematic errors, of existing data, have been achieved. In addition, new and ongoing analyses of SPS data, most notably from NA60 [6, 7] (including low- and intermediate-mass dileptons and J/ψ production), have reached unprecedented levels of precision that now can distinguish between model predictions which were consistent with earlier data sets. Furthermore, questions have been re-opened that a few years ago seemed to be essentially settled (e.g., the energy-loss mechanism for jet quenching). It therefore appears fair to say that whereas the *existence* of the new form of matter has been established, we neither understand its *microscopic properties* nor deduced convincing signals of the *phase transition* itself. Theory also made substantial progress in the last few years by moving from more signal-specific explanations to a coherent description by connecting different phenomena and improving theoretical tools, but a widely accepted “grand scheme” encompassing both bulk and microscopic components has not been realized. As ideas get refined (largely steered by data), different theoretical predictions often approach each other, thus increasing the demand on higher quality measurements to differentiate between them.

After a very successful operation of RHIC¹ and its detectors over the first five years of data taking we are approaching a point where further progress requires improved experimental capabilities. Table 1 lists important physics topics that are either beyond our current reach or would be significantly enhanced with the indicated detector and luminosity upgrades. These should be put into context with overarching questions in the investigation of the sQGP and chiral/deconfinement transitions, which include (with emphasis on where electromagnetic probes are particularly relevant):

- What are the temperatures and corresponding system sizes of thermalized matter

¹By 2004 (Run-4) the accelerator exceeded design luminosities by a factor of 2.5 both in $Au+Au$ and $p+p$ collisions; it collided 4 different systems including the asymmetric $d+Au$, and did so at 6 different *cms* energies, including 19GeV ($Au+Au$) and 22 GeV ($Cu+Cu$), establishing overlap with CERN-SPS.

Upgrades	High T	QCD...	QGP		Spin		Low-x
	e+e-	heavy flavor	jet tomog.	quarkonia	W	$\Delta G/G$	
PHENIX							
Hadron blind detector	X						
Vertex Tracker	X	X	O	O		X	O
Muon Trigger				O	X		
Forward Cal (NCC)			O	O	O		X
STAR							
Time of Flight (TOF)	X	O	X	X			
Heavy fl. tr. (HFT)	X	X		X			
Forward Tracker		O			X	O	
Forward Cal (FMS)						O	X
DAQ 1000	O	O	X	X	O	O	O
RHIC Luminosity	O	O	X	X	O	O	O

Table 1

Matrix of detector or accelerator upgrades vs. physics measurements. X = upgrade critical for measurement. O = upgrade important for measurement.

at its early stages?

- How do hadron properties change in hot and dense matter, and how are hadron masses generated? How do the medium modifications depend on temperature and net/total baryon density?
- Can we deduce signatures of Chiral Symmetry Restoration (χ SR), and if so, how is it realized?
- What are the relevant degrees of freedom in the sQGP? Does it harbor bound states and/or resonances?
- How do the medium properties change if the net baryon density is increased? Can a QCD critical point be found?
- How does the system reach (local) equilibrium on the apparently short time scales required by hydrodynamics?
- What exactly causes jet quenching?

In the remainder of this introductory section, we will first elaborate in somewhat more detail on the features and strongholds of e.m. probes in heavy-ion collisions (Sec. 1.2); in particular, we will give a discussion of the achievements and shortcomings of the e.m. probes program at the SPS (Sec. 1.3) which will help us to sharpen the case for future RHIC measurements. In Sec. 2 we lay out the theoretical framework for describing and interpreting e.m. probes; we will also provide predictions for observables and formulate

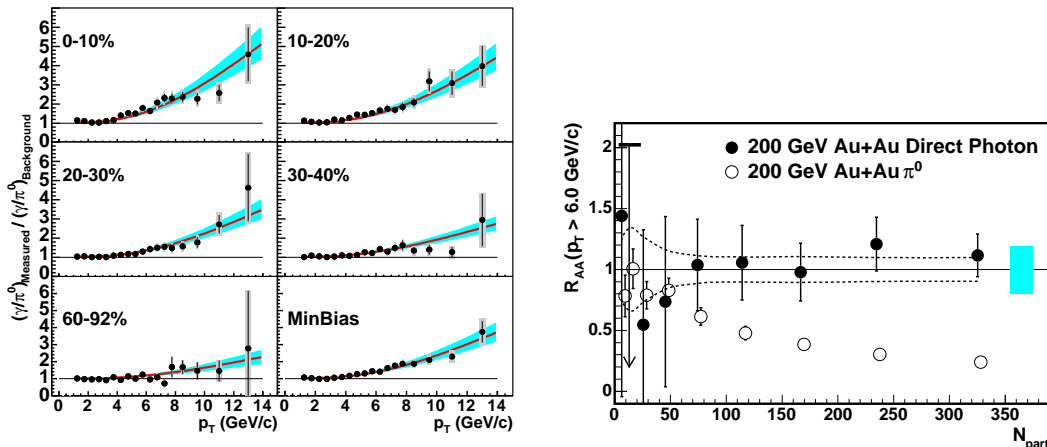


Figure 1. Left panel: direct photon excess ratios for $\sqrt{s_{NN}}=200\text{GeV}$ $Au+Au$ collisions [8]. The curves are the ratios predicted by NLO pQCD [9]. Right panel: integrated R_{AA} for photons and π^0 s as a function of centrality for $\sqrt{s_{NN}}=200\text{GeV}$ $Au+Au$ collisions.

strategies for deducing information on key properties of the medium that may not follow from an immediate interpretation of experimental data. In Sec. 3 we give a brief overview on the current status of e.m. observables at RHIC. In Sec. 4 we then focus on how future detector and accelerator can be used and geared for answering the above listed questions. In Sec. 5 we reiterate the main points of this document.

1.2. Where EM Probes Are Unique or Very Important

Electromagnetic probes are real (γ) and virtual photons (dileptons l^+l^- , $l=e, \mu$); due to their negligible final-state interaction with the strongly interacting medium they are emitted from the entire reaction volume throughout the evolution of a heavy-ion collision, from first impact in primordial (hard) $N-N$ collisions until late decays of long-lived hadrons (long after strong interactions have ceased). *Direct* photon spectra are defined as the spectra remaining after subtraction of final-state decays (“background” or “decay photons”), whereas in measured dilepton spectra the latter are usually included and assessed separately being referred to as the “hadronic decay cocktail”.

Unfortunately, the same property that allows photons to escape freely ($\alpha_{EM} \ll \alpha_s$) also leads to major experimental challenges - low rates and large backgrounds from the above mentioned late hadron decays (Dalitz-decays and $\pi^0 \rightarrow \gamma\gamma$, $\eta \rightarrow \gamma\gamma$, ...).

The fact that direct photons from initial hard scattering escape freely [8] is demonstrated in Fig. 1, where the measured direct photon excess ratio at sufficiently high transverse momentum, p_T , is shown to be consistent with next-to-leading order (NLO) perturbative QCD (pQCD) calculations, even in the most central $Au+Au$ collisions. The interesting physics that we are primarily concerned with in this report is situated at significantly lower p_T and dilepton invariant masses, M_{ll} . This is not easily gleaned from Fig. 1 which already at this level illustrates one of the major points that we will repeatedly encounter: the importance of precision data at masses and momenta below $\sim 3\text{-}4$ GeV.

Electromagnetic probes are **unique** in

- giving direct access to the in-medium modifications of hadronic states (vector mesons $\rho(770)$, $\omega(782)$, $\phi(1020)$) via dilepton invariant-mass spectra, which can illuminate the nature of hadron mass generation and thus the origin of $\sim 98\%$ of the visible mass in the universe (as well as related changes in the structure of the QCD vacuum including the restoration of chiral symmetry). In addition, at masses above $\sim 1\text{ GeV}$ there exists the possibility of detecting novel nonperturbative (resonant) correlations in a sQGP.
- inferring the temperature of the system during its hottest phases via direct thermal radiation of photons and dileptons radiation; additional HBT interferometry of thermal photons offers the cleanest measurement of early system sizes.

Indirect consequences of the above studies include insights into the mechanism of (rapid) thermalization (e.g., via resonance formation in the sQGP) and a determination of the effective degrees of freedom if a temperature measurement is complemented with independent information on the energy or entropy density. Although not unique, e.m. probes are valuable to (i) disentangle the energy loss mechanism of jets (jet quenching) by inferring photon radiation off energetic quarks, as well as establishing the jet-energy scale in γ -hadron jets. (ii) obtain complementary information on (early) matter flow by investigating (the p_T -dependence of) photon elliptic flow (v_2), which in turn facilitates to discriminate thermal photons from those radiated off jets.

In the following sections, we will elaborate these statements together with the requirements to measure associated observables with sufficient accuracy.

1.3. Theory vs. Experiment at the CERN-SPS

Before we go into a more detailed discussion of the theoretical aspects underlying a comprehensive electromagnetic probes program for future RHIC runs, let us briefly review the main achievements at the SPS until recently (except the new NA60 data [6, 7] which we will return to below). An example of an overall comparison of e.m. emission in semi-/central $Pb+Au/+Pb$ is compiled in Figs. 2 and 3. The upshot is that of a common thermal source with an initial temperature of $T_0 \simeq 210 \pm 30$ MeV and a lifetime of about 12 ± 3 fm/c before reaching a thermal freezeout temperature of around 100-120 MeV. Importantly, the low-mass dilepton enhancement in the CERES e^+e^- data [33] (upper left panel) requires substantial medium effects on the ρ -meson spectral function (and sufficient lifetime as quoted above), but a decisive discrimination between a dropping-mass scenario [42] and a massively broadened spectral function [40] could not be accomplished; the level of the QGP contribution is small, around 10-15%. The sensitivity to QGP radiation increases in intermediate-mass dimuon spectra of NA50 [37], where the observed factor-2 excess over baseline charm and Drell-Yan sources can be reasonably accommodated with thermal radiation containing a 30% (maybe up to 50%) [41, 44, 43] QGP component, which is the main evidence for the above quoted initial temperature. A very similar decomposition is found in the WA98 direct photon spectra [38] in the $q_t \simeq 2$ GeV region. The recently published low-momentum data points [39], extracted via photon HBT methods, are not easily reconciled with theoretical predictions, although the inclusion of soft Bremsstrahlung off $\pi\pi$ and πK scattering appears to improve the

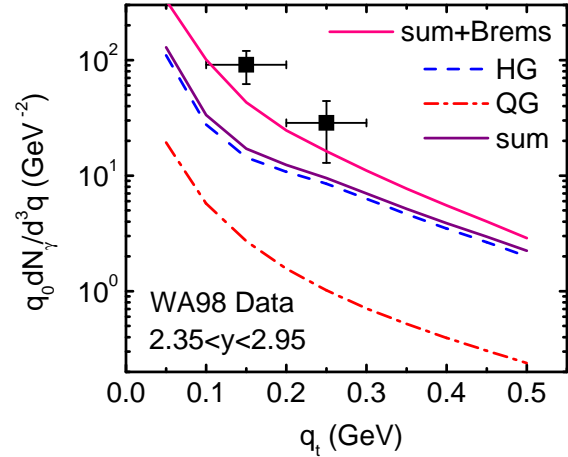
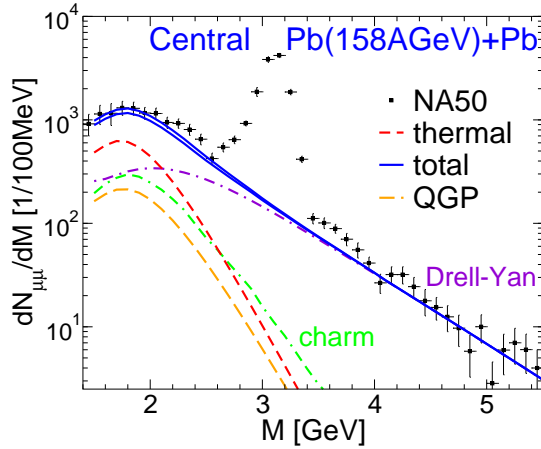
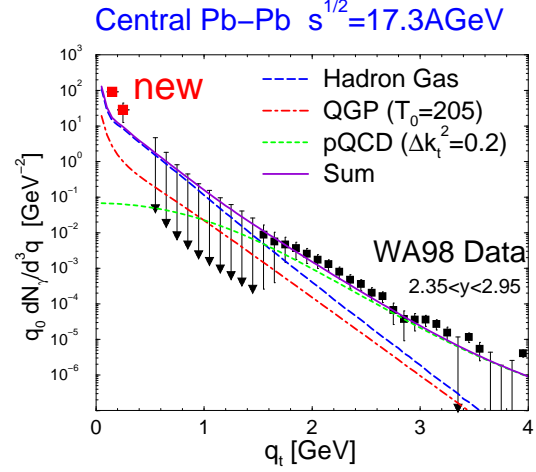
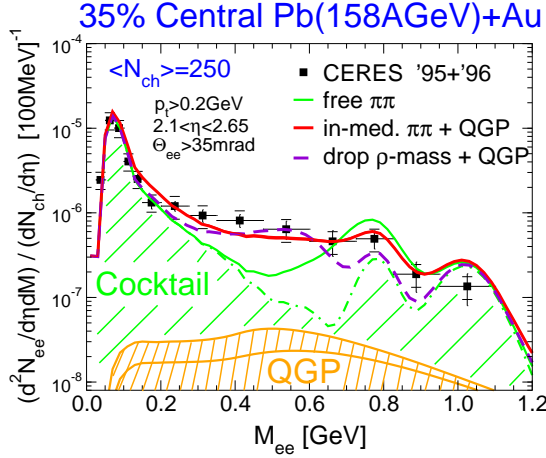


Figure 2. Dilepton spectra at the SPS compared to calculations [40, 41] within an expanding thermal fireball model. Upper panel: low-mass dielectrons of CERES/NA45 [33]; lower panel: intermediate-mass dimuons of NA50 [37]

Figure 3. Direct photon spectra of WA98 [38, 39] at the SPS compared to thermal emission within the same fireball model as in Fig. 2 with the e.m. correlator as used for dileptons but carried to the photon point [45, 46].

situation [46] (the low-momentum yield is essentially proportional to later stages of the fireball evolution, and thus to its total lifetime).

The question thus arises: What was lacking in the EM Probes program at the SPS? Several items are to be mentioned:

- (a) no decisive discrimination of in-medium modifications of the ρ meson (although this has been much improved by recent NA60 data [6, 7], albeit in a smaller system, see below), in particular no systematic excitation function in terms of an energy scan (there was one low-energy run by CERES/NA45 at $E_{lab} = 40$ AGeV [47] indicating an increase over the enhancement at 160 AGeV, but with large errors);

- (b) no definite determination of the Cronin enhancement in the primordial pQCD photons which is essential for an accurate assessment of the thermal photon yield in the $q_t \simeq 2$ GeV, region;
- (c) no explicit identification of charm dileptons which hampers the temperature extraction in the intermediate-mass dimuon spectra (again, NA60 made substantial progress for an intermediate-size system);
- (d) no experimental redundancy to cross-check measurements and create competition;
- (e) after all, there remains the possibility that the QGP contribution at SPS is too modest *in principle* to reveal itself in a significant way;
- (f) early thermalization at SPS may not be sufficient to justify thermal approaches in the early phases, as could be indicated by a lack of elliptic flow in hadron data relative to hydrodynamic models above $p_T \sim 1.5$ GeV.

We will argue below that *all* of these issues can be (are) overcome at RHIC-2.

2. THEORETICAL CONSIDERATIONS AND PREDICTIONS

2.1. Objectives and Framework

Ample evidence for (early) thermalization of the matter formed in (semi-/central) $\sqrt{s_{NN}} = 200$ GeV $Au+Au$ collisions from current RHIC data provides the necessary prerequisite to validate the notion of studying the QCD phase diagram. So far, most of the deduced features pertain to bulk matter properties, including large (energy-) densities (ϵ) well above the critical one extracted from lattice QCD [12].

In the following subsections, we will sketch a theoretical framework that provides the basis to gain decisive new insights according to the following 3 subject areas:

- Temperature Measurement

Explicit temperature extractions are so far restricted to hadro-chemical and -thermal freezeouts. The goal is to establish early temperatures (well) above T_c , which is feasible with photons and dileptons at a typical energy/momentum/invariant-mass scale of 1-3 GeV. Together with information on the energy and/or entropy density, this enables to access the effective number of degrees of freedom, d_{of} , using $\epsilon = \frac{\pi^2}{30} d_{of} T^4$ or $s = \frac{2\pi^2}{45} d_{of} T^3$ [79, 16, 18].

- Vector-Meson Spectral Functions

To extract microscopic information on the constituents of the medium, invariant-mass spectra of dileptons are invaluable and unique. Modifications of low-mass vector mesons ($V = \rho, \omega, \phi$) in hot and/or dense hadronic matter have been extensively studied theoretically (see Refs. [28, 29, 30, 31, 32] for reviews), largely triggered by the intriguing excess radiation observed at the CERN-SPS [33, 7]. At RHIC, for the first time, these measurements will be performed in an environment that is close to *net* baryon-free, which will provide important tests of the relevant mechanisms underlying predicted medium effects. In addition, the higher initial temperatures achieved at RHIC will open much more direct access to radiation from the (s)QGP

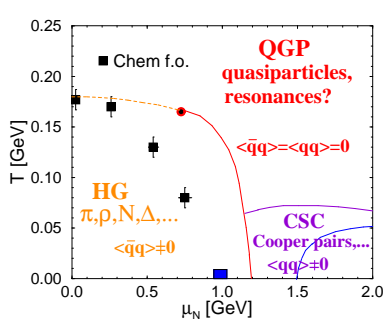


Figure 4. Schematic phase diagram of QCD including temperature “measurements” from chemical analysis of produced hadrons [13].

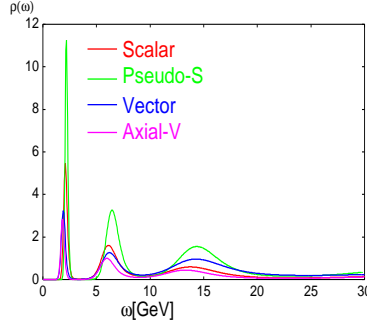


Figure 5. “Light” hadronic spectral functions in the QGP ($T=1.4T_c$) from lattice QCD [14], exhibiting resonances with approximate chiral symmetry.

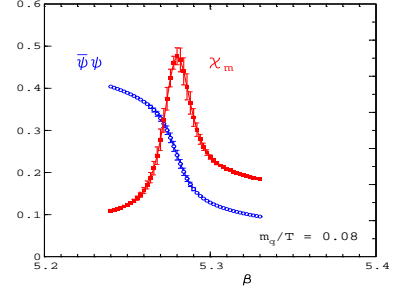


Figure 6. Temperature dependence of the chiral quark condensate, $\langle \bar{q}q \rangle(T)$, as computed in unquenched lattice QCD [15].

and thus be sensitive to suggested resonance/bound-state formation above T_c in the vector channel [27]. This is to be compared to more indirect probes of resonances, e.g., quantitative analyses of energy loss [17] and elliptic flow in hadron spectra (especially in the charm sector [25]), or systematics of charmonium regeneration [26].

- The Origin of Mass and Chiral Symmetry Restoration

A more ambitious goal is to infer signatures of the phase transition (or rapid crossover) which requires the study of order parameters. For the chiral transition, these are, e.g., quark condensates, the constituent quark mass or the pion decay constant, none of which is a (viable) observable. However, the condensate structure of the (finite-temperature) ground state is encoded in its (hadronic) excitations. The objective is thus to establish connections between the in-medium vector correlator measured in dilepton spectra and order parameters.

All of the above items are inevitable consequences of QGP formation, albeit mostly non-perturbative in nature. While data interpretation will require the application of model approaches, well-defined links to finite-temperature lattice QCD computations and symmetry (as well as phenomenological) constraints will be essential to deduce meaningful evidences.

We emphasize that thermal production rates for photon and dilepton spectra can be cast into a uniform theoretical framework according to

$$q_0 \frac{dN_\gamma}{d^4x d^3q} = -\frac{\alpha_{\text{em}}}{\pi^2} f^B(q_0; T) \text{Im}\Pi_{\text{em}}^T(q_0 = q; \mu_B, T) , \quad (1)$$

$$\frac{dN_{e^+e^-}}{d^4x d^4q} = -\frac{\alpha_{\text{em}}^2}{M^2 \pi^3} f^B(q_0; T) \text{Im}\Pi_{\text{em}}(M, q; \mu_B, T) , \quad (2)$$

where the key quantity is the (imaginary part of) the (retarded) electromagnetic correlation function, Π_{em} [35, 36]. In the vacuum, this function can be measured in e^+e^-

annihilation and decomposes into two regimes: at masses above $M = \sqrt{q^2} \simeq 1.5 \text{ GeV}$, the strength of the e.m. spectral function, $\text{Im}\Pi_{\text{em}}^{\text{vac}}$, is rather accurately determined by perturbation theory, i.e., the annihilation into $q\bar{q}$ (with little impact from subsequent hadronization), while at low mass the cross section is saturated by the light vector meson ρ , ω and ϕ (vector dominance model), i.e. nonperturbative resonance formation:

$$\text{Im}\Pi_{\text{em}}^{\text{vac}}(M) = \begin{cases} \sum_{V=\rho,\omega,\phi} \left(\frac{m_V^2}{g_V}\right)^2 \text{Im}D_V(M) & , M < 1.5 \text{ GeV} \\ -\frac{M^2}{12\pi} \left(1 + \frac{\alpha_s(M)}{\pi} + \dots\right) N_c \sum_{q=u,d,s} (e_q)^2 & , M \geq 1.5 \text{ GeV} . \end{cases} \quad (3)$$

For thermal dilepton emission this implies that, on the one hand, the low-mass region carries information on dynamical medium effects with a relative strength of the vector mesons approximately given by 11:1:2 for $\rho:\omega:\phi$ (reflecting the vector-dominance couplings, (m_V^4/g_V^2) , or, equivalently, the decay widths into dileptons). On the other hand, at intermediate mass a reasonably controlled emission strength provides the basis for probing the temperature. As it turns out [34], the temperature and volume dependence in space-time integrated dilepton spectra combine in a way that the prevalent contribution at low mass originates from temperatures around and below T_c , whereas at high mass (energy) the exponential sensitivity of the Bose factor strongly biases contributions toward high temperatures. Similar considerations apply to transverse-momentum spectra of thermal photons. This corroborates the feasibility of the 3 basic objectives listed above. Also note that the leading-order contribution to the dilepton rate is $\mathcal{O}(\alpha_s^0)$ (applicable at sufficiently large invariant mass, $M > 1.5 \text{ GeV}$), while a nonzero photon rate requires processes at least at $\mathcal{O}(\alpha_s)$.

In rough accordance with the above physics objectives, we adopt the following classification of regimes in dilepton invariant mass, M_{ll} (or photon transverse momentum, q_t):

- low-mass region (LMR), $0 < M_{ll} < 1.1 \text{ GeV}$ (V -meson decays)
- intermediate-mass region (IMR) (continuum radiation, QGP emission, resonances?)
- high-mass region (HMR) (primordial emission and heavy quarkonia)

2.2. QCD Lattice Results

Thermal dilepton rates have been studied in lattice QCD within the quenched approximation [48]. The computation of the finite-temperature Euclidean correlators in the vector channel is supplemented by a transformation into the time-like regime using the maximum entropy method, after which the dilepton rate follows from eq. (2). The results for zero 3-momentum at 2 different temperatures above T_c are compared to calculations in perturbation theory [49] in Fig. 7. The lattice rates are quite comparable to the perturbative ones at high energy, while the enhancement at intermediate $\omega \simeq 5T$ could be related to resonance formation in the QGP. Toward small energies, the lQCD rates drop substantially and deviate markedly from the perturbative calculations, which in the HTL approximation even diverge. Being a loop effect (nontrivial order in α_s), the HTL divergence is closely related to a non-vanishing thermal photon rate. Recent lattice

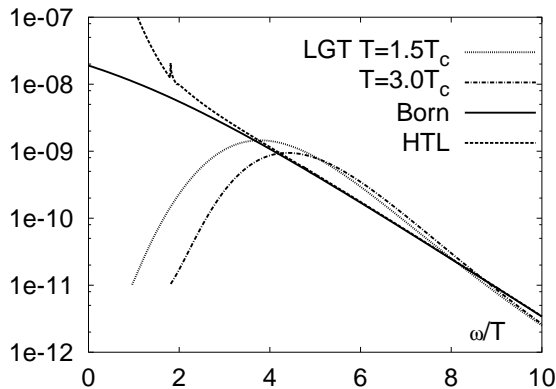


Figure 7. Thermal dilepton production rates in the QGP as evaluated in quenched lattice gauge theory (LGT) at zero 3-momentum (dotted and dash-dotted line) [48]. The solid and dashed line are pQCD calculations of the rate in Born approximation ($q\bar{q}$ annihilation to leading order, $\mathcal{O}(\alpha_s^0)$) and with hard-thermal-loop corrections [49], respectively.

computations of the vector correlator at finite 3-momentum [50, 51] confirm that the rates in Fig. 7 lead to vanishing photon emission. If this (seemingly unrealistic) feature is induced by lattice artifacts, the decrease of the dilepton rate toward small ω may not uphold either, leading to better agreement with HTL extrapolations (and thereby affect the interpretation of the "resonance" structure). The (ultra-) soft limit of the e.m. correlator can be further studied by its relation to the electric conductivity, σ_{em} , via the Kubo formula,

$$\sigma_{\text{em}}(T) = \frac{e^2}{3} \frac{\partial}{\partial q_0} \text{Im} \Pi_{\text{em}}^T(q_0, q = 0; \mu_B, T) . \quad (4)$$

The correlators found in Ref. [48] correspond to a vanishing conductivity, but a different method employed in Ref. [52] leads to a finite (rather large) value of $\sigma_{\text{em}}(T) \simeq 7 \sum e_q^2 T$, cf. the discussion in Ref. [51]. It would be very interesting to compare this result to the conductivity underlying the soft photon emission rates as used in the description of the low-momentum WA98 data [39] in the lower panel of Fig. 3. A step in this direction has recently been undertaken in Ref. [53], where σ_{em} has been evaluated in a low-temperature pion gas within chiral perturbation theory.

Another interesting source of information are susceptibilities associated with conserved quantum numbers, i.e., derivatives of the (thermodynamic) free energy with respect to a chemical potential,

$$\chi_X = - \frac{\partial^2 \Omega}{\partial \mu_X^2} . \quad (5)$$

These have recently been evaluated in lattice QCD for quark and isospin chemical potentials [54]. When extrapolated into the finite- μ_q plane, the quark susceptibility develops a maximum structure while the isospin one stays monotonous. Since the susceptibilities can be related to the space-like static limit of the corresponding correlation function (in ω and

ρ channels, respectively), valuable information on the soft part of the spectral functions may be inferred [55] (or at least tested for a given model).

2.3. Sum Rules

Besides direct lQCD calculations of dilepton and photon rates (which, for unquenched simulations, are not anticipated for the near and midterm future), model-independent information (and constraints for effective models) is encoded in (energy-weighted) sum rules relating (integrated moments of) spectral functions to vacuum expectation values of composite quark and gluon operators (“condensates”), or (partial) conservation laws of (axial-) vector currents. These sum rules are thus prime examples of connecting hadronic excitations to the underlying ground-state structure (symmetry-breaking pattern), including order parameters. We will briefly discuss two classes thereof.

2.3.1. QCD Sum Rules

QCD sum rules (QCDSRs) [56] are based on the analyticity of correlation functions which enables to formulate a pertinent dispersion relation,

$$\int d\omega \frac{\text{Im}\Pi_{\text{em}}(\omega)}{\omega - q_0} = \sum_n \frac{C_n}{Q^{2n}}. \quad (6)$$

The left-hand-side (*lhs*) involves an integral over a (hadronic) spectral function in the timelike regime (plus possible subtractions not indicated here); the right-hand-side (*rhs*) is an expansion in (spacelike) momenta, $1/Q^2$ ($Q^2 \equiv -q^2 > 0$), with leading perturbative terms and nonperturbative effects encoded in Wilson coefficients C_n via quark and gluon condensates of increasing dimension (with n). When applied to the light vector mesons ρ and ω at finite temperature and/or density, it turns out that the largest sensitivity resides in the medium dependence of the 4-quark condensates, $\langle(\bar{q}q)^2\rangle$. Unfortunately, rather little is known about their temperature dependence from lattice QCD so far. The usual assumption is to factorize the 4-quark condensates into a product of 2-quark condensates corresponding to the assumption of ”ground-state dominance”, with an extra parameter κ representing correlation effects (which is usually fixed in the vacuum). An application of QCDSRs to the ρ meson in cold nuclear matter is shown in Fig. 8 [59], indicating that the finite-density decrease of the condensates mandates a ”softening” of the ρ spectral function. The required low-mass enhancement can be satisfied by an increasing width, a decreasing mass, or a suitable combination thereof as indicated by “allowed regions” enclosed by the bands in the right panel of Fig. 8 (cf. also Refs. [57, 58], as well as [60] for a recent update).

2.3.2. Chiral Sum Rules

Chiral sum rules (CSRs) [61, 62] have been derived prior to QCD from current algebra and chiral Ward identities. The (partial) conservation of the (axial-) vector-isovector currents leads to relations between the pion decay constant, $f_\pi = 92$ MeV (an order parameter of chiral symmetry breaking), to moments of differences between pertinent

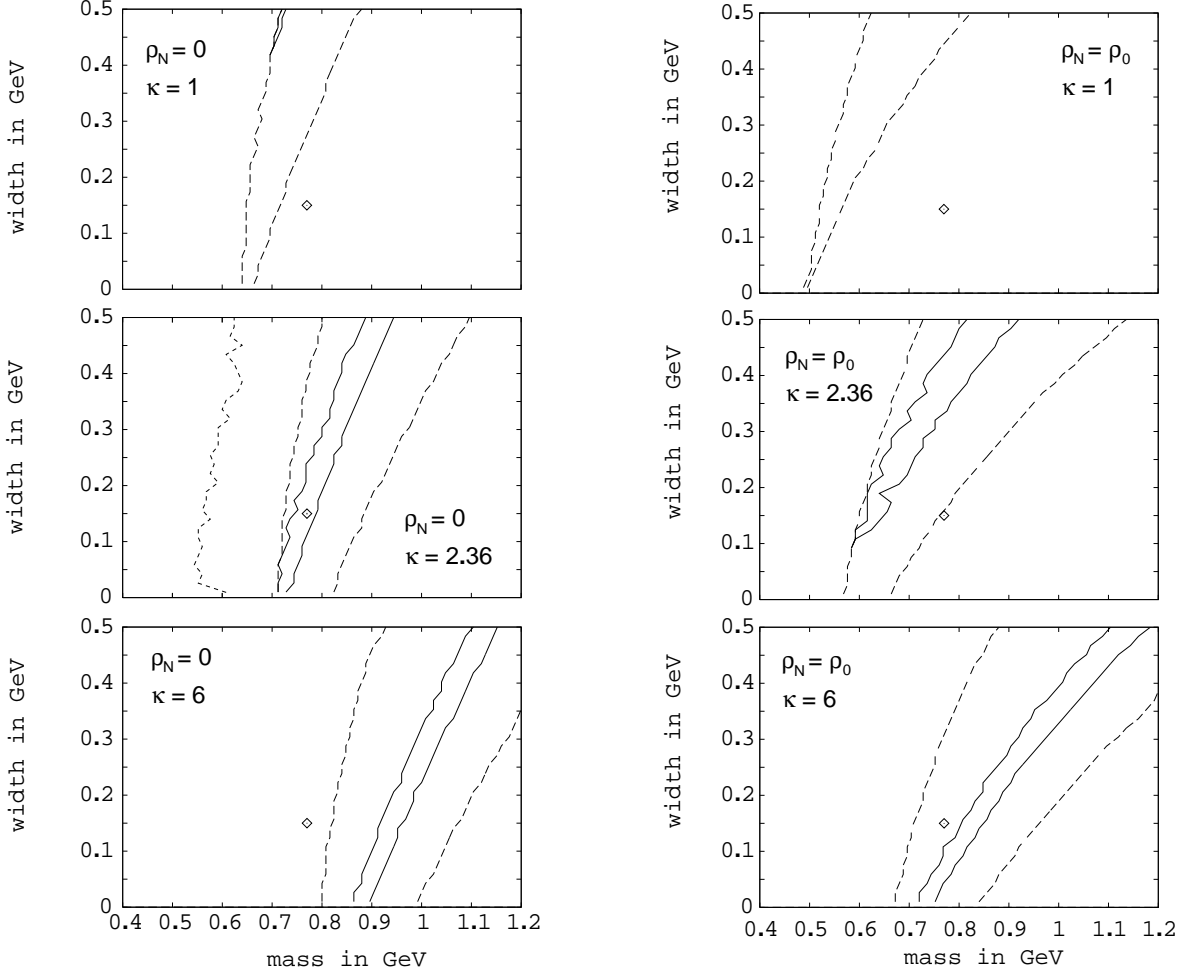


Figure 8. QCD sum rule constraints on Breit-Wigner ρ -meson spectral functions in the mass-width plane [59]. The bands indicate regions of mass and width values for which the deviation of the *lhs* from the *rhs* in eq. (6) is below 0.2% (within the solid lines) or below 1 % (within the dashed lines). The left column is for the vacuum case which is used to determine the "correlation parameter" κ in the 4-quark condensate (diamond: mass and width of the free ρ meson).

spectral functions. In vacuum they read²

$$\int_0^\infty \frac{ds}{s^2} [\rho_V^{\text{vac}}(s) - \rho_A^{\text{vac}}(s)] = f_\pi^2 \frac{\langle r_\pi^2 \rangle}{3} - F_A \quad (7)$$

$$\int_0^\infty \frac{ds}{s} [\rho_V^{\text{vac}}(s) - \rho_A^{\text{vac}}(s)] = f_\pi^2 \quad (8)$$

²The form of the sum rules as written above applies to the chiral limit (vanishing current light-quark and pion masses). Corrections to the second Weinberg Sum Rule (WSR), eq. (9), have been discussed, e.g., in Refs. [63, 64, 65], and may not be small; the first WSR, eq. (8), seems not to be affected.

$$\int_0^\infty ds [\rho_V^{\text{vac}}(s) - \rho_A^{\text{vac}}(s)] = 0 \quad (9)$$

$$\int_0^\infty s ds [\rho_V^{\text{vac}}(s) - \rho_A^{\text{vac}}(s)] = -2\pi\alpha_s \langle \mathcal{O} \rangle, \quad (10)$$

where $\langle r_\pi^2 \rangle$ is pion charge radius squared, F_A the axialvector form factor in the radiative pion decay ($\pi \rightarrow l\bar{\nu}_l\gamma$), and the vacuum axial-/vector spectral functions are

$$\rho_{V,A}^{L,T} = -\frac{1}{\pi} \text{Im} \Pi_{V,A}^{L,T}. \quad (11)$$

In eq. (10), which was obtained in Ref. [66], $\langle \mathcal{O} \rangle$ denotes a 4-quark condensate (e.g., in the factorization approximation it assumes the value $(16/9)\langle \bar{q}q \rangle^2$). The direct connection of the CSRs to the vector correlator renders them particularly valuable in the context of dilepton production. The assessment of in-medium effects requires their extension to finite temperature which has been elaborated in Ref. [66]. Due to loss of Lorentz invariance when specifying the thermodynamic rest frame, the original vacuum results become energy sum rules at fixed 3-momentum and split into longitudinal (L) and transverse (T) components of the correlators and quark condensate,

$$\int_0^\infty \frac{dq_0^2}{(q_0^2 - q^2)} \Delta\rho^L(q_0, q) = 0 \quad (12)$$

$$\int_0^\infty dq_0^2 \Delta\rho^{L,T}(q_0, q) = 0 \quad (13)$$

$$\int_0^\infty q_0^2 dq_0^2 [\Delta\rho^L(q_0, q) + 2 \Delta\rho^T(q_0, q)] = -4\pi\alpha_s [\langle\langle \mathcal{O}_\mu^\mu \rangle\rangle + 2 \langle\langle \mathcal{O}^{00} \rangle\rangle]. \quad (14)$$

where $\Delta\rho \equiv \rho_V - \rho_A$, and $\langle\langle \cdot \rangle\rangle$ denotes an in-medium expectation value. The transverse and longitudinal components of the spectral functions are given in terms of standard projection operators,

$$\rho_{V,A}^{\mu\nu} = \rho_{V,A}^T P_T^{\mu\nu} + \rho_{V,A}^L P_L^{\mu\nu}, \quad (15)$$

where the pionic piece (which in vacuum takes the form $\rho_\pi^{\mu\nu} = f_\pi^2 q^2 \delta(q^2) P_L^{\mu\nu}$) has been included in the longitudinal axialvector channel (in medium, the pion spectral function is subject to medium modifications as well). The in-medium Weinberg-type sum-rules (12)-(14) impose stringent constraints on both temperature and energy-momentum dependencies (through the moments) of (chiral hadronic) models for vector and axialvector spectral function. The (model-independent) connection to lattice QCD can be implemented by employing pertinent temperature dependencies of pion decay constant and four-quark condensates which, in principle, are easier to compute than full spectral functions.

We now turn to a more concrete discussion and examples on how to realize the 3 main points outlined at the beginning of this Section.

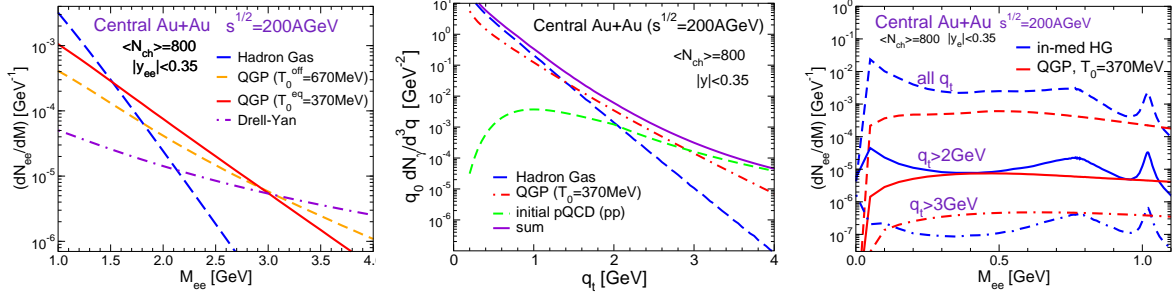


Figure 9. Comparison of electromagnetic emission spectra from QGP and HG at intermediate invariant mass / transverse momentum in central $Au+Au$ collisions at full RHIC energy. Left panel: IMR dileptons [67] including primordial Drell-Yan annihilation; middle panel: direct photons [45] including primordial pQCD contributions; right panel: low-mass dileptons imposing cuts on the pair transverse momentum. (Note that the IMR dilepton spectrum on the *lhs* does not include contributions from the ϕ -meson nor a cut on the *single*-electron rapidity; the latter is the main source of the difference to the LMR spectrum on the *rhs* which, in turn, does not include dilepton emission from 4π and higher states which dominates the hadronic emission beyond the ϕ -mass region.)

2.4. Temperature and Degrees of Freedom

2.4.1. Suitable Kinematic Regimes

Thermal emission rates for electromagnetic radiation, eqs. (1) and (2), can in principle be used to “infer” the temperature of thermalized matter in heavy-ion collisions if (i) the emission strength represented by the e.m. correlator is reasonably well determined (so that the T dependence essentially resides in the Bose factor), (ii) a kinematic window can be identified where radiation from a reasonably well-defined temperature regime prevails. Ideally, these conditions are met at the highest masses/energies, where the correlators can be reliably evaluated in pQCD and thermal emission from the earliest phases exponentially dominates. In practice, however, the high-mass/energy region is dominated by dileptons/photons from primordial (hard) $N-N$ collisions, whereas toward low mass the contributions from lower temperatures increase substantially (a more comprehensive discussion of the various sources will be given below).

Fig. 9 gives an example for a set of predictions for space-time integrated photon and dilepton spectra at intermediate masses and/or transverse momenta in central $\sqrt{s_{NN}} = 200$ AGeV $Au+Au$ collisions [67, 45]. The thermal spectra are decomposed into QGP and hadronic emission from an isentropically expanding thermal fireball assuming a critical temperature of $T_c=180$ MeV [69] (with total entropy fixed to reproduce the observed hadron multiplicities at chemical freeze-out, $(\mu_N^{ch}, T_{ch})=(25,180)$ MeV). pQCD photon rates (to leading order in α_s [68]) and HTL-resummed dilepton rates [49] are convoluted over a chemically equilibrated QGP assuming a formation time of $\tau_0=1/3$ fm/c translating into $\bar{T}_0=370$ MeV (670 MeV if the initial parton-densities are assumed to be undersaturated); uncertainties in the longitudinal expansion, affecting the QGP lifetime, can induce changes of the QGP spectra of up to 30%, while the sensitivity to τ_0 is larger, especially

at masses above 2 GeV [67]. The hadronic emission spectra include in-medium modifications of the e.m. correlator (see Sec. 2.5 for details) as well as chemical off-equilibrium in the hadronic evolution until thermal freeze-out (see Sec. 2.6). Three regimes emerge where QGP radiation outshines both HG and primordial emission:

- (i) 3-momentum integrated dilepton spectra at intermediate mass, $M \simeq 1.5 - 3$ GeV;
- (ii) direct photon spectra at intermediate transverse momentum, $q_t \simeq 1.5 - 3$ GeV;
- (iii) low-mass dilepton spectra at transverse momenta above $q_t \simeq 2$ GeV (“low-virtuality” photons).

Of course, in practice a careful assessment of additional sources, including “pre-equilibrium” contributions and jet-plasma interactions (such as Bremsstrahlung off quark jets or Compton scattering of gluon jets) [85, 86], is mandatory before firm conclusions on the thermal component can be drawn (it should be noted, that the above predictions for thermal photon spectra together with jet-plasma interactions and primordial photons extracted from p - p collisions compare favorably with preliminary RHIC data for direct photons [70], see also below). Recent calculations of the jet-plasma component suggest that the latter exceeds thermal emission for transverse (real and virtual) photon momenta $q_t \geq 3 - 4$ GeV [85, 86].

2.4.2. Direct Photons and Current RHIC Data

To illustrate uncertainties and required precision in a “temperature measurement”, we discuss in this section an analysis of the most recent direct photon spectra in central 200 GeV $Au+Au$ at RHIC. The left panel of Fig. 10 compiles several model calculations of thermal photon production (mostly based on hydrodynamic evolutions, in which case the maximal initial temperature is quoted): Srivastava *et al.* [19] (with initial conditions $\tau_0 \approx 0.2$ fm/ c and $T_0 = 450$ -660 MeV), Alam *et al.* [20] ($\tau_0 = 0.5$ fm/ c , $T_0 = 300$ MeV)³, Räsänen *et al.* [23] ($\tau_0 = 0.17$ fm/ c , $T_0 = 580$ MeV), Turbide *et al.* [45] (expanding fireball with $\tau_0 = 0.33$ fm/ c , $\bar{T}_0 = 370$ MeV) and d’Enterria and Peressounko [18] ($\tau_0 = 0.15$ fm/ c , $T_0 = 590$ MeV); cf. also Steffen and Thoma [22] ($\tau_0 = 0.5$ fm/ c , $\bar{T}_0 = 300$ MeV). For similar initial conditions, the total thermal yields in these calculations are compatible with the data and with each other within a factor of ~ 2 . On the one hand, this confirms the dominant role of thermal radiation in the window $q_t \simeq 1.5$ -3 GeV, but, on the other hand, in-depth comparisons are required (and, in principle, feasible), disentangling the underlying assumptions on evolution model (boost-invariant hydrodynamics with or without transverse expansion, thermal fireballs, etc.) and productions rates, to narrow down the viable range of initial temperatures. The excess over the expectation from primordial N - N collisions (commonly denoted as “prompt” contribution) is better illustrated by the “nuclear modification factor”, R_{AA}^γ , defined as the ratio of the total (direct) photon spectra over binary-collision scaled p + p pQCD predictions,

$$R_{AA}^\gamma(p_T) = \frac{dN_{AuAu}^{total \gamma} / dp_T}{T_{AA} \cdot d\sigma_{pp}^{\gamma pQCD} / dp_T}, \quad (16)$$

³Alam *et al.* have recently [21] recomputed their hydrodynamical yields using higher initial temperatures ($T_0 = 400$ MeV at $\tau_0 = 0.2$ fm/ c) to improve the agreement with the data.

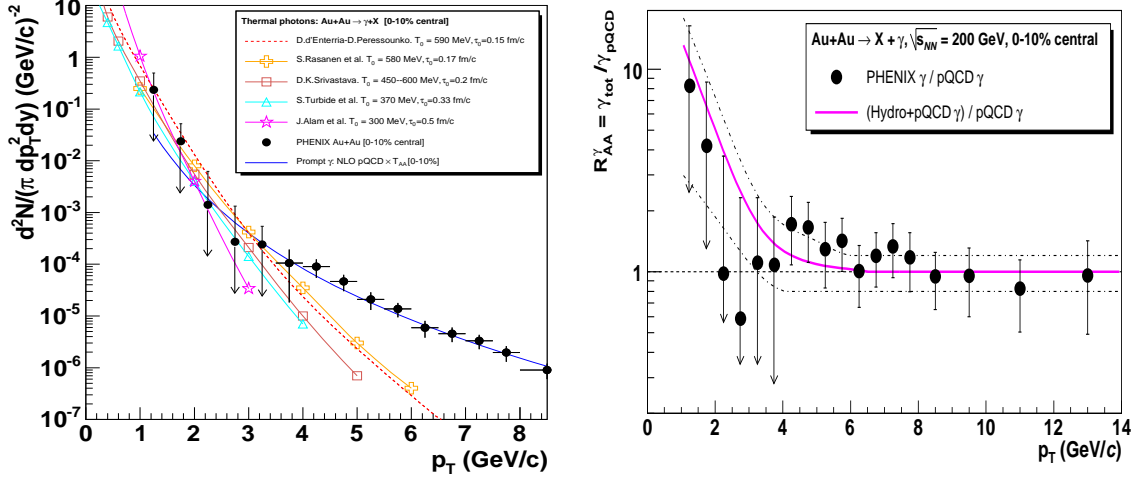


Figure 10. Left panel: Thermal photon spectra for central $Au+Au$ reactions at $\sqrt{s_{NN}}=200$ GeV as computed within different models (see text), compared to the expected pQCD prompt γ yields (T_{AA} -scaled NLO $p+p$ calculations [9], solid line without symbols) and to the experimental total direct photon spectrum as measured by PHENIX [8]. Right panel: Direct photon “nuclear modification factor”, eq. (16), for 0-10% most central $Au+Au$ reactions at $\sqrt{s_{NN}}=200$ GeV. The solid line is the ratio resulting from a hydro+pQCD model [18], the points show the PHENIX data [8] over the same NLO yields, and the dashed-dotted curves indicate the theoretical uncertainty of the NLO calculations.

($T_{AA}(b)$: nuclear overlap function at impact parameter b), as displayed in the right panel of Fig. 10. The data are consistent with the existence of a significant excess over the next-to-leading order (NLO) pQCD expectations (which in turn describe the $p-p$ data), but it should be emphasized that below $q_t \approx 4$ GeV it is not yet clear to what extent the NLO predictions, entering in the denominator of eq. (16), are applicable. In this regime the theoretical prompt yields are dominated by jet bremsstrahlung as determined from the parametrized parton-to-photon GRV form factor [24] which is relatively poorly known at the pertinent q_t . The standard scale uncertainties in the NLO pQCD calculations are $\pm 20\%$ above $q_t \approx 4$ GeV but could become as large as ${}_{+50}^{-200}\%$ for $q_t \approx 1-4$ GeV, as indicated by the dashed-dotted lines in the right panel of Fig. 10. Obviously, precise measurements of the direct- γ baseline spectra in $p+p$ and $d+Au$ collisions at $\sqrt{s}=200$ GeV above $q_t=1$ GeV are an essential component in quantifying a thermal signal from $Au+Au$ collisions.

The measurement of the slope of the resulting thermal photon spectrum, T_{eff} does not directly reflect the temperature of the hot matter, as photons are emitted throughout the space-time volume of the evolving matter implying varying temperatures, as well as blue shifts due to collective expansion. Nevertheless, a correlation between the apparent photon slope and the (maximum) temperature attained in the system persists, cf., e.g., the recent study within a hydrodynamical model in Ref. [18]. The measured T_{eff} then provides an empirical link to the effective number of degrees of freedom of the system via $d_{of} = \frac{30}{\pi^2} \epsilon / T_{\text{eff}}^4$

or $d_{of} = \frac{45}{2\pi^2} s/T_{\text{eff}}^3$ [18]. The initial (maximal) energy or entropy density are difficult to access experimentally. Indeed, all available observables related to the initial ϵ and s such as the total transverse energy, the total particle multiplicity, or the colored-particle density encountered by quenched jets on their path through the medium, are related to space-time averaged quantities. Yet, information on the temperature dependence of d_{of} can be obtained via centrality and $\sqrt{s_{NN}}$ dependencies. It has been argued in Ref. [18] that, at the minimal level, it is possible to discriminate a QGP-like equation of state with fixed number of d_{of} above T_{crit} from a hadronic resonance gas with a rapidly rising number of degrees of freedom, by establishing the dependence of T_{eff} on the pseudo-rapidity density of the charged particles. As a further consistency check, one can employ the suggestion of Ref. [16] relating the degrees of freedom to suitable powers of energy and entropy densities, $d_{of} \propto s^4/\epsilon^3$.

2.4.3. Chemical Off-Equilibrium

While a rapid thermalization of the matter at full RHIC energy is fairly well established, its composition in terms of quark and gluon degrees of freedom (chemical equilibration) is much less clear (as are the equilibration mechanisms themselves).⁴ From the prevalence of gluons in the relevant x -range of the incoming nuclei at mid-rapidity, one might expect the early matter to be a gluon plasma (GP), as is routinely assumed, e.g., in calculations of jet-quenching in terms of radiative energy loss [71]. However, recent calculations of $q\bar{q}$ pair production within the classical fields generated by the incoming Au nuclei indicate a rather fast approach to chemical equilibrium [72]. This, in turn, would have important consequences for disentangling the relevant mechanism(s) for energy loss of fast partons (with a significant reduction of radiative energy loss due to the smaller color-charge of anti-/quarks). The apparently obvious test of these questions is via electromagnetic probes which maximally distinguish between gluons and anti-/quarks (with electric charge zero and 1/3 or 2/3, respectively), as has been studied by several authors [73, 74, 75, 76, 67]. From LO pQCD processes ($q + g \rightarrow \gamma + X$, $q\bar{q} \rightarrow l^+l^-$) in a thermal, but chemical off-equilibrium, QGP one anticipates the photon and dilepton production rates to scale with $\lambda_g \lambda_{q,\bar{q}}$ and $\lambda_q \lambda_{\bar{q}}$, respectively, where λ_i denote fugacities characterizing the deviation of the parton densities from the chemical-equilibrium limit (for the latter, $\lambda_q = \lambda_{\bar{q}} = \lambda_g$); e.g., at RHIC, a typical GP initial state with subsequent evolution using inelastic pQCD reaction rates starts from $\lambda_g \simeq 1/3$, $\lambda_{q,\bar{q}} < 0.1$ evolving to values around or larger than 0.5 [77, 76, 78]. However, in an isentropic expansion with fixed initial entropy, undersaturated matter implies significantly higher initial temperatures at otherwise identical conditions; e.g., for central $Au+Au$ at RHIC, with a thermalization time of $\tau_0 = 1/3$ fm/c, one finds $T_0^{\text{eq}} \simeq 370$ MeV vs. $T_0^{\text{off}} \simeq 670$ MeV. It turns out that for photon spectra the reduced fugacities in the emission rate are largely compensated by the higher temperatures in the QGP evolution with only a slight hardening of the slope parameter [79]. For thermal dilepton spectra, this effect appears to be more pronounced, cf. the left panel of Fig. 9. Disentangling a hardening of the slope as evidence for a GP at RHIC is further complicated by the fact that the thermal yields are still fairly sensitive to the assumed thermalization time, τ_0 . However, a decrease in τ_0 in chemical equilibrium will not only decrease the slope

⁴The expansion in hydrodynamic simulations is mostly driven by the ratio of pressure to energy density, P/ϵ , in which the number of degrees of freedom essentially drops out.

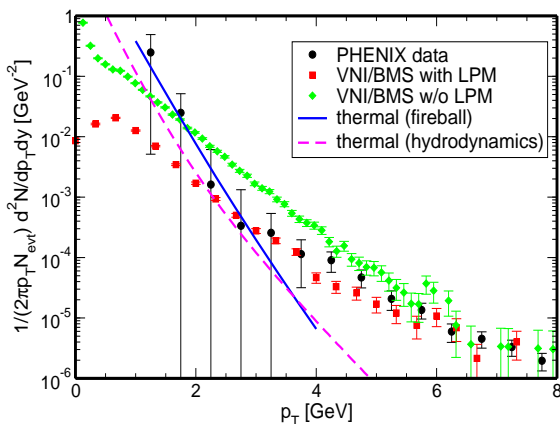


Figure 11. Comparison of (early) photon emission from a parton cascade simulation for central 200 AGeV $Au+Au$ [81] with (squares) and without (diamond) LPM interference effects. Also shown are expanding fireball [82] and hydrodynamic [83] calculations of thermal photons, as well as preliminary data from PHENIX [84].

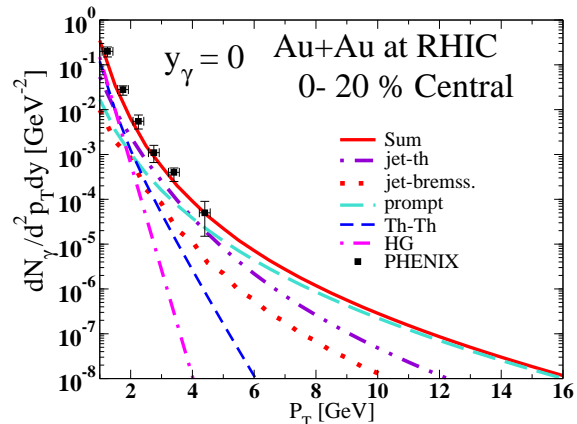


Figure 12. Predictions for direct photon spectra combining pQCD initial, jet-plasma interactions [85] as well as thermal radiation [45], compared to preliminary PHENIX data [70]. (The lines labeled "Th-Th" and "HG" correspond to the usual thermal radiation from QGP and hadron gas, respectively.)

of the thermal spectrum but also lead to an overall increase of the yield. Identifying a GP (or more generally, the number of degrees of freedom above T_c) from thermal dileptons will thus have to involve a quantitative assessment of *both* slope and absolute magnitude of the thermal spectrum, after "removal" of non-thermal sources including Drell-Yan, and, more importantly correlated open-charm decays as well as pre-equilibrium and jet-plasma interactions. In the following section we briefly summarize recent progress on the latter two.

2.4.4. Pre-Equilibrium and Jet-Plasma Emission

Dilepton emission subsequent to the initial (hard) $N-N$ collisions but before the assumed thermalization time (the so-called pre-equilibrium contribution) can be addressed in a parton cascade approach. A corresponding calculation [80] has predicted rather large emission yields, which, in fact, overestimate preliminary PHENIX data [84] (cf. Fig. 11). However, upon inclusion of Landau-Pomeranchuk-Migdal (LPM) interference effects, the yield is appreciably suppressed [81], indicating that the combined initial pQCD plus pre-equilibrium yield is not very different from the pQCD contribution alone (Fig. 11), with the thermal yield taking over for momenta below $q_t \simeq 2.5$ GeV (quite reminiscent to the middle panel of Fig. 9). Also note that the calculations of the thermal spectra in Fig. 11 agree reasonably well with the one in the middle panel of Fig. 9. However, the present model dependencies will have to be further reduced to achieve enough sensitivity to discern the composition of the early matter and realize the desired temperature measurement.

Fig. 12 shows predictions for a combination of direct photons from initial pQCD, jet-

plasma interactions [45], as well as thermal QGP and HG radiation [45] (from the middle panel of Fig. 9) evaluated within the same expanding fireball. The comparison to preliminary low- q_t PHENIX data [70] is quite encouraging; in this calculation, jet-plasma contributions exceed the thermal yield already close to $q_t \simeq 2$ GeV, implying a rather narrow “QGP window”. Note, however, that the thermal and jet-induced radiation are not independent contributions as both are affected by the parameters characterizing the QGP (lifetime and temperature or number and energy density), which imposes an additional consistency requirements.

2.5. In-Medium Spectral Functions below and above T_c

In the mid 1990’s, dilepton data from the CERN-SPS have triggered vigorous theoretical activity in trying to assess modifications of vector-meson properties in hot/dense (mostly hadronic) matter. The focus has been on the ρ meson due to its prevalent role in the dilepton emission, see, e.g., Refs. [28, 29, 30, 31, 32] for rather recent reviews. In Secs. 2.5.1 and 2.5.2 below, we briefly summarize some of the main features and insights that have emerged over the last ~ 10 years.

2.5.1. Hadronic Many-Body Theory and Chiral Virial Expansion

Effective hadronic models for vector mesons should be compatible with basic symmetry principles (electromagnetic gauge invariance, vector-current conservation, chiral symmetry⁵). In addition, it is essential that the underlying effective vertices are carefully constrained by phenomenological information such as hadronic and electromagnetic decay widths or scattering data (particularly valuable are, e.g., photoabsorption data on both nucleons and nuclei [87, 88], which provide information on in-medium effects up to nuclear matter density).

Most of the effective models with constraints built along the above lines have reached a reasonable degree of agreement, which generically predict a substantial broadening in matter with little mass shift⁶. This applies to calculations both in cold nuclear matter [89, 58, 90, 91, 92], and in hot and dense matter [40, 93] (cf. Fig. 13 for an example). Effective models also suggest that the effects of the baryonic component of the medium dominate over those from the mesonic one at comparable density (which is also consistent with findings in large- N_c QCD where meson-meson interactions are suppressed relative to meson-baryon ones).

The broadening of the spectral functions, amounting to a total width of ~ 500 MeV at nuclear matter saturation density and typically accompanied by a slight *upward* mass shift (cf. left panel of Fig. 14), is in fair agreement with constraints from QCD sum rules [59] (recall Fig. 8 above). When extrapolated to temperatures and densities close to the expected chiral transition, an almost complete “melting” of the ρ -resonance structure emerges. This is not only true for the net-baryon rich regime at SPS energies and below, but also in the central rapidity region at collider energies where the baryon chemical po-

⁵In many instances, especially if no pions are involved, little is known about the chiral structure of both baryonic and mesonic resonance couplings.

⁶A simple argument to understand this feature is that imaginary parts of (in-medium) self-energies, which govern the broadening, are negative definite ($\text{Im}\Sigma < 0$) and therefore strictly add up, whereas real parts, which induce mass shifts, change sign around a resonance. Real parts therefore tend to cancel if the system is characterized by a rich excitation spectrum, as is the case for hadronic resonance gas.

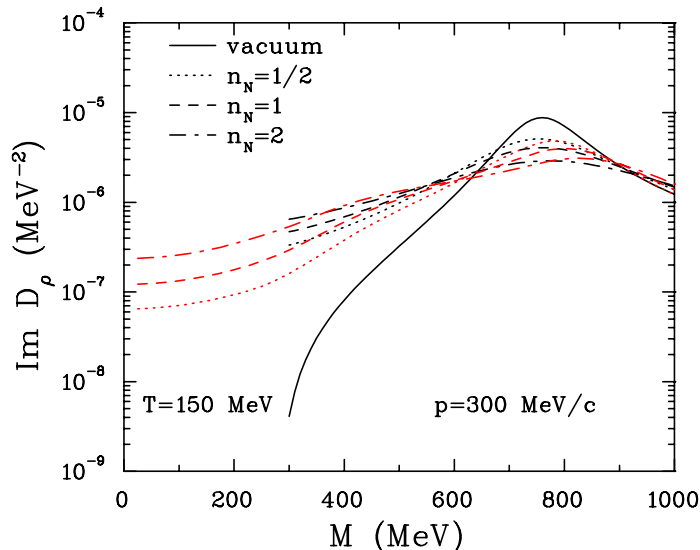


Figure 13. Comparison of ρ meson spectral functions in hot hadronic matter within the many-body calculation of Ref. [40] (red lines, extending to $M=0$) and an approach based on (imaginary parts of) ρ -hadron scattering amplitudes (supplemented by dispersion relations to obtain the real parts) [93] (black lines). Reasonable agreement under conditions relevant for heavy-ion experiments is observed.

tential is small, cf. middle panel of Fig. 14. The reason is [67] that at the experimentally extracted chemical freezeout temperature (e.g., $T_{\text{ch}} \simeq 180$ MeV at RHIC), an appreciable density of baryon-antibaryon ($B\bar{B}$) pairs is thermally excited, and that mesons equally interact with baryons and antibaryons (also note that the notion of chemical freeze-out implies that baryon-antibaryon annihilation in the subsequent hadronic evolution is suppressed). Thus, the relevant quantity for medium effects on V -mesons is the sum of (or *total*) B and \bar{B} density, which, close to T_{ch} , is quite comparable at $\mu_B=0$ and $\mu_B=250$ MeV⁷. The baryon-density effects on the ρ are most pronounced at masses below ~ 0.5 GeV, rather than at the free mass and above (compare long-dashed and short-dashed lines in the middle panel of Fig. 14). On the contrary, the ϕ -meson appears to be less sensitive to the baryonic component of the medium, although this conclusion may change once a better understanding of recent (photon- and proton-induced) ϕ -meson production data off nuclei has been achieved [94, 95].

The ρ (and possibly ω) “melting” has interesting implications that deserve further theoretical investigations:

- (i) The very short mean-free-path of the ρ -meson (and other hadrons) close to T_c is suggestive for the formation of a hadronic liquid [96] which opens the possibility

⁷Experimentally, the total baryon rapidity density, $dN_{B+\bar{B}}/dy(y=0)$, is indeed very comparable at maximal SPS ($\sqrt{s}=17.3$ GeV) and RHIC ($\sqrt{s}=200$ GeV) energies; the total hadron rapidity density (mostly due to pions) is a factor of ~ 2 larger at RHIC, implying an accordingly lower total baryon density at the transition; however, most of the pertinent medium effects on the ρ spectral function build up at densities at or below ϱ_0 , cf. left panel of Fig. 14.

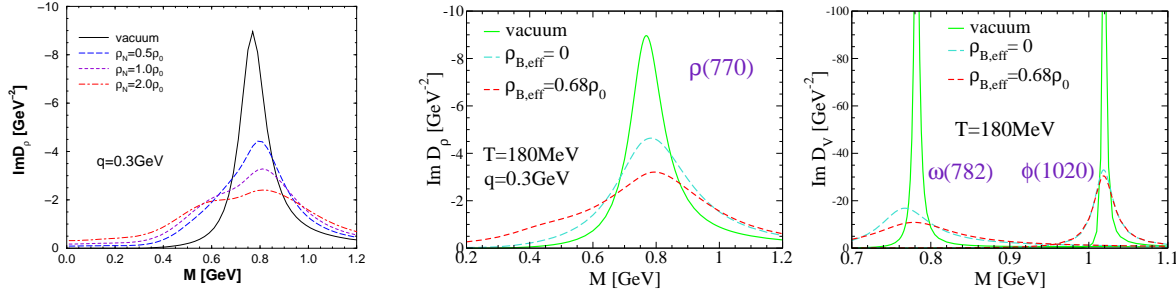


Figure 14. In-medium V -meson spectral functions within hadronic many-body theory. Left panel: ρ meson in cold nuclear matter at various densities in units of the saturation density, $\rho_0=0.16 \text{ fm}^{-3}$. Middle panel: ρ -meson under RHIC conditions close to T_c with and without the effect of anti-/baryons [67]. Right panel: same as middle panel but for ω and ϕ [67].

that, from the structural point of view, the matter properties in the phase transition region change rather smoothly, from a hadronic liquid to a sQGP liquid.

- (ii) The hadronic in-medium e.m. correlator (based on the “melted” ρ meson) is surprisingly close in shape and magnitude to the QGP correlator evaluated in HTL pQCD [49] at *all* masses [40, 97]; again, this is suggestive for a rather continuous transition from HG to QGP close to T_c , even on the level of spectral functions. The approximate coincidence, while not understood theoretically, of the bottom-up and top-down extrapolated hadronic and pQCD calculations enhances the confidence in applying these emission rates in fireball/hydro evolutions across T_c (as is inevitable in every calculation of a space-time integrated thermal dilepton spectrum).

Similar conclusions on the ρ -meson also emerge within the chiral virial approach [88], where the medium effects on the vacuum vector correlator are evaluated within a pion- and nucleon-density expansion coupled with vacuum V - π and V - N scattering amplitudes constrained by chiral symmetry: the ρ -meson peak is quenched (even though not broadened) and its low-mass shoulder is substantially enhanced, mostly due to the impact of baryons in the heat bath [98]. This agreement, at least at low and moderate densities/temperatures, is again a consequence of the constraints imposed on the underlying hadronic interactions.

2.5.2. Dropping Mass

Models involving dropping vector-meson masses [99] have recently been revisited within the so-called vector manifestation of chiral symmetry [31, 100, 101]. Using the Hidden Local Symmetry (HLS) framework, where the mass of the ρ -meson is generated via a Higgs mechanism, an alternative representation of the chiral group as been proposed in which the chiral partner of the pion is identified with the longitudinal ρ meson (rather than with the “ σ ” channel as in the conventional scenario). This approach leads to a satisfactory vacuum phenomenology, and a renormalization group analysis with hadronic loop effects reveals a fixed point with vanishing vector-coupling constant. When applied to the finite- T chiral phase transition, a matching of the vector and axialvector correlators to the operator

product expansion (space-like q^2) requires a vanishing of the bare ρ -meson mass (becoming degenerate with the pion mass) which persists when carried on-shell due to the fixed-point nature of the transition. It is also found that the vector dominance model (VDM), which works well in the vacuum, is violated at finite T (although not necessarily [101]), suppressing $\pi\pi$ annihilation to dileptons via intermediate rho mesons (being replaced by direct annihilation via intermediate photons). The latter feature renders the observation of a dropping ρ mass in dilepton spectra difficult and has been argued as a way to reconcile the new NA60 data [6, 7] with a dropping-mass scenario. However, no vector spectral functions nor dilepton rates in the vector manifestation approach are available yet.

A question remains in how far the Higgs mechanism for the ρ -mass at the hadronic level is appropriate. E.g., at the quark-antiquark level, interactions in the vector channel are rather weak (the ρ -meson mass is close to twice the constituent quark mass), and finite temperature effects leading to an enhanced interaction and accordingly reduced ρ mass are not easily conceived [102] (see Ref. [104] for an alternative view). Furthermore, it has not yet been worked out how the presence of hadronic many-body effects (especially baryons), as discussed in the previous section, affects the matching procedure and resulting axial-/vector spectral functions.

2.5.3. Resonances in the sQGP

Another interesting development that can possibly relate to measurements of electromagnetic probes are the conjectured hadronic bound states in the (s)QGP [103, 105]. The possibility to detect signatures of the vector states in the dilepton spectrum hinges on whether their mass is sufficiently large, $M_V(T \geq T_c) > 1 \text{ GeV}$. As emphasized subsequent to eq. (3), only at these masses can QGP radiation compete (or overcome) the contributions of the longer-lived (and larger-volume) hadronic phase, especially if the resonance structure is moving with temperature. The lattice QCD (lQCD) spectral functions and dilepton rates shown in Figs. 5 and 7, respectively, indeed indicate resonances with masses in the $M \simeq 2 \text{ GeV} \simeq 10T_c$ regime, roughly scaling with temperature. Theoretically, the existence of these states may be understood [103] as being due to heavy quark-quasiparticles bound by a rather strong color Coulomb-type attraction as is also operative in charmonium (or bottomonium) states (in this case, heavy-quark symmetry implies approximate degeneracy of vector (“ ρ ” or J/ψ) and pseudoscalar states (“ π ” or η_c), while the connection to the pions becoming (almost) massless when approaching T_c from above is less obvious).

The quantitative signature of the vector resonances above T_c in the dilepton spectrum has been elaborated in Ref. [27]. When convoluting the T -dependent resonance decays over an expanding fireball model at RHIC [67, 69] an enhancement over the baseline pQCD emission scenario ($q\bar{q}$ annihilation) of about a factor ~ 2 has been predicted, see Fig. 15. This result bears noticeable sensitivity to the vector-meson width (smaller widths lead to narrower peaks and thus a stronger enhancement over the pQCD spectrum) which in turn is governed by the width of the quark quasi-particles. The latter is expected to be around 0.1-0.2 GeV based on self-consistent solutions of a $q\bar{q}$ scattering equation [105] using as input interaction potentials from finite- T lQCD. The corresponding elastic scattering rates of 0.5-1/(fm/c) are suggestive for the short thermalization times deduced from hydrodynamic analyses of elliptic flow measurements, and therefore could provide a

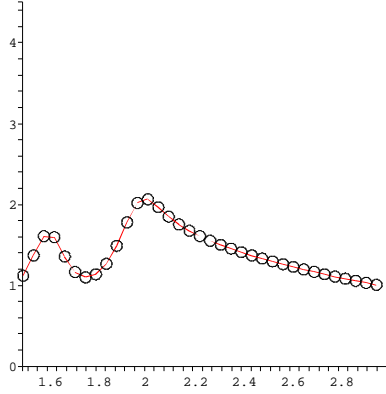


Figure 15. Ratio of dilepton spectra at RHIC from a resonance-enhanced rate to perturbative $q\bar{q}$ annihilation [27] (as obtained from QGP and mixed phase of an expanding thermal fireball [67, 69]). The first (second) peak represents the mass of the vector state close to T_c (from the vicinity of the "zero-binding" line for $T \simeq 1.5 - 2T_c$). The x -axis is in units of the quark-quasiparticle mass ($M_q \simeq 1\text{GeV}$); the quark-quasiparticle width has been assumed to be 0.1 GeV [105].

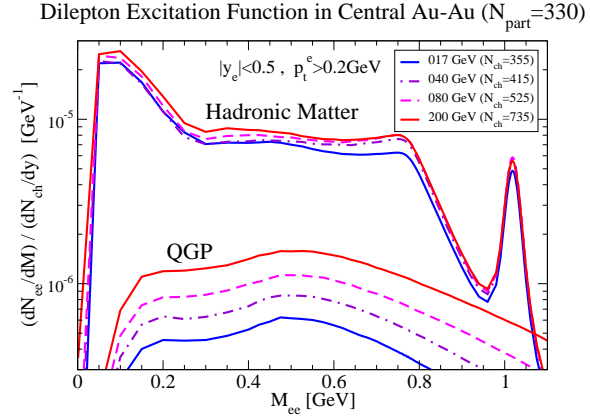


Figure 16. Excitation function of low-mass dilepton spectra for central $Au+Au$ collisions from top SPS to top RHIC energy. The upper (lower) set of 4 curves corresponds to thermal radiation from hadronic matter (QGP) using in-medium ρ , ω and ϕ spectral functions [40, 69] (HTL $q\bar{q}$ annihilation [49]), assuming a critical temperature between 175 MeV ($\sqrt{s} = 17\text{ AGeV}$) and 180 MeV ($\sqrt{s} > 100\text{ AGeV}$).

link to the early thermalization puzzle at RHIC.

2.6. Low-Mass Dilepton Spectra

To illustrate the predictions of medium-modified vector mesons within effective models, and in particular to investigate the importance of the baryonic component of the medium, we summarize in Fig. 16 a pertinent excitation function of low-mass dilepton spectra in central $Au+Au$ collisions. Thermal dilepton rates in QGP [49] and HG [40, 67] phases are convoluted over the an isentropic fireball evolution similar to those underlying Figs. 9 and 15, assuming a chemically equilibrated QGP which converts into a chemically equilibrated HG at (μ_N^c, T_c) -values compatible with: (i) thermal models for hadron production in central $A-A$ collisions [13], and (ii) a total entropy to reproduce available data on particle multiplicities [2, 3, 4]. The hadronic evolution subsequent to chemical freeze-out is augmented by effective chemical potentials for hadrons that are stable under strong interactions (e.g., π , K , η , baryons and antibaryons). This is mandatory to maintain the observed chemical composition until thermal freeze-out [119] and, in particular, implies sizable $total (B+\bar{B})$ baryon densities in the later stages of the hadronic evolution (recall Sec. 2.5.1). The somewhat surprising result is that there is no appreciable change in both shape and magnitude of the (hadronic) dilepton-spectrum excitation function for

$\sqrt{s}=20\text{-}200$ GeV. The main reasons for this situation are:

- (i) Despite the large range in baryo-chemical potentials ($\mu_B^c=25\text{-}250$ MeV at chemical freezeout, with a small variation in $T_c=175\text{-}180$ MeV), and thus in net baryon density, the (prevalent) baryon-induced medium effects are comparable once the sum of B and \bar{B} density is properly accounted for.
- (ii) the lifetime of the hadronic (and mixed) phase changes little since the larger volume expansion at higher energies is essentially compensated by an increase in radial flow as inherited by the QGP phase.

This scenario has to be contrasted with one where the medium effects are sensitive to *net* baryon density (as, e.g., in simple parameterizations of dropping masses, $m_V^*/m_V = (1 - C\rho/\rho_0) \times (1 - (T/T_c)^2)^{1/n}$). In the latter case, a stronger variation of the excitation function is anticipated, with *weaker* effects at higher collision energy. As to be expected from larger initial temperatures and QGP lifetimes, QGP emission increases appreciably with \sqrt{s} but remains subdominant ($\leq 20\%$) in the low-mass region at all energies (if no significant cut on q_t is applied).

At masses above ~ 1 GeV, the e.m. spectral function is dominated by 4π and higher contributions (encompassing annihilation reactions of type $\rho+\rho$, $\pi+\omega$, πa_1 , etc.). These are not included in the hadronic phase in Fig. 16, but may become significant at masses starting around $M \simeq 0.9$ GeV, where a corresponding enhancement could be related to effects of (partial) chiral symmetry restoration [107, 108]. We will return to this issue in Sec. 2.7.2 below.

Finally, a few remarks on space-time evolution models are in order, which, after all, provide the (crucial) input of the thermodynamic parameters for the equilibrium e.m. emission rates. Hydrodynamical models are obviously the approach of choice (since formulated in the same variables as thermal emission rates), if applicable. RHIC data so far suggest that ideal hydrodynamics is a good approximation for the first ~ 5 fm/ c (after thermalization), encompassing QGP, “mixed” phases and possibly the early hot+dense hadronic liquid phase for $T \geq 150$ MeV or so. For lower temperatures, however, effects of viscosity are expected to become significant [122]. It is presently not clear in how far these affect dilepton (and photon) emission calculations; the underlying uncertainties have to be scrutinized, since especially the low-mass/-momentum spectra receive significant contributions from the later evolution stages. The choices are then to either implement viscosity effects into hydrodynamics (to still keep the notion of thermodynamic variables), or to switch to transport theoretical descriptions [123, 124, 125]. In the latter option, it is a rather nontrivial task to properly implement broad resonances [126], but an alternative could be to extract local temperatures and (baryon-) densities in the transport simulations and convolute those with the equilibrium e.m. emission rates. The degree of agreement of this method with (viscous) hydrodynamics could then serve to judge the uncertainties on the level of the integrated e.m. spectra (and justify a posteriori fireball models which after all are suitable parameterizations of microscopic evolution models). Such a procedure will become particularly relevant if one computes less penetrating probes, e.g., $\pi\pi$ or $\pi\gamma$ invariant-mass spectra (as discussed below). Especially in the vicinity (or for the treatment) of thermal freeze-out, transport-based approaches are mandatory to quantitatively

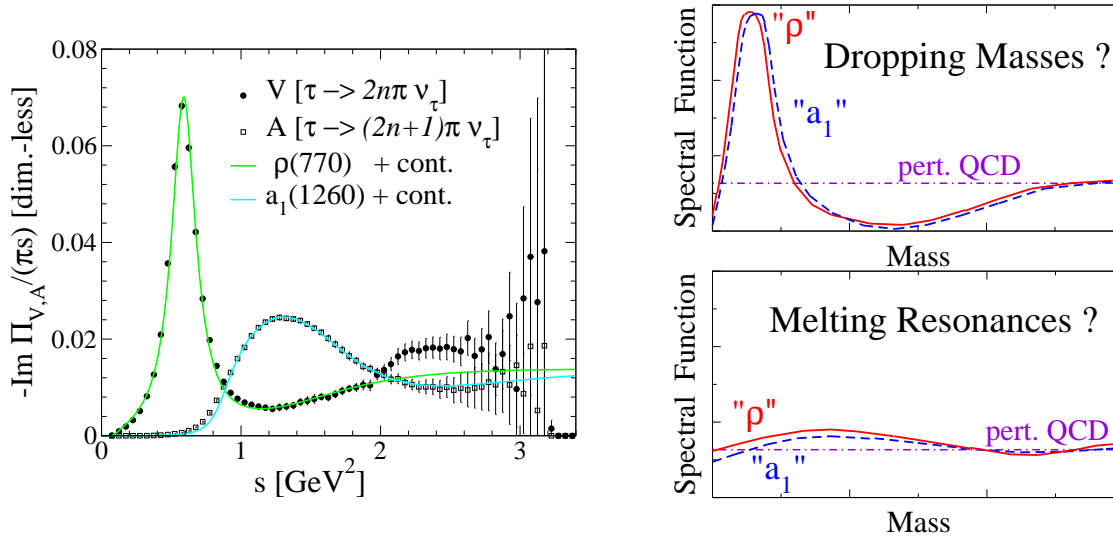


Figure 17. Left panel: vector and axialvector spectral functions in the vacuum as measured in hadronic τ decays [120] with model fits using ρ and a_1 resonances plus perturbative continua [121]; right panel: two schematic scenarios for chiral symmetry restoration in hot and dense matter.

account for finite sizes, times and mean-free-paths. In the late 1990's, in the context of the CERES low-mass dileptons [33] at the SPS, the agreement between hydrodynamic [127], transport [128] and fireball models [40, 129] has been reasonable, albeit with somewhat limited theoretical and experimental precision.

2.7. Chiral Symmetry Restoration

2.7.1. Direct and Indirect Approach

We now address the question how, in principle, in-medium effects detected in dilepton spectra can be converted into conclusions on (the approach to) chiral symmetry restoration (χ SR). An unambiguous consequence of the latter is that (isovector-) vector and axialvector correlation functions, which are very different in the vacuum, degenerate at and beyond the chiral transition - the question is *how* this happens, see Fig. 17 for an illustration. We emphasize again that the effects of chiral symmetry breaking are concentrated at low masses (already in vacuum, the correlators degenerate in the pQCD regime) and therefore constitute an inherently nonperturbative phenomenon which requires input from both experiment and theoretical model approaches.

A direct way to assess χ SR is a *measurement* of the in-medium axialvector spectral function in connection with model comparisons as done for dileptons. In Ref. [113] it has been suggested to attempt this by measuring $\pi^\pm\gamma$ invariant-mass spectra. This was partly motivated by similar first measurements of $\pi^+\pi^-$ invariant-mass spectra in heavy-ion collisions which indicated interesting modifications of the ρ -meson in the late stages of (peripheral) 200 AGeV $Au+Au$ collisions RHIC [114]. Absorption effects on the outgoing pions limit the information in $\pi\pi$ spectra to rather dilute stages, while $\pi\gamma$ spectra probe, in principle, somewhat denser stages. However, emission from later stages

in the collision has the advantage that a smaller window in density and temperature of the source is probed so that the convolution over the space-time history becomes less of an issue. Experimentally the challenge are the rather low rates (even though the radiative decay branching ratio of the a_1 is rather small, the (not so small) absolute decay width $\Gamma_{a_1 \rightarrow \pi\gamma} \simeq 0.7$ MeV is the relevant quantity for thermal radiation), as well as the rather broad structure of the $a_1(1260)$ resonance (~ 0.4 GeV even in vacuum) which makes it susceptible to distortions due to background subtractions; this will be studied in more detail including explicit simulation results in Sec. 4.2.2 below.

In addition to the direct experimental approach to the axialvector channel, we now formulate a well-defined theoretical procedure based on chiral hadronic models to bridge the experimental information on the vector correlator (dileptons) to (first-principle) information on chiral restoration from lattice QCD. A pivotal ingredient are the in-medium versions of the chiral sum rules, eqs. (12), (13) and (14), as follows:

- (1) Calculate vector (V) and axialvector (A) spectral functions as a function of temperature and density (including as many of the constraints mentioned above as possible) in a chirally invariant model.
- (2) Insert the results into Weinberg sum rules to evaluate the temperature dependence of pion decay constant and 4-quark condensate, and compare to results from lattice QCD (note that $f_\pi(T)$ and $\langle(\bar{q}q)^2\rangle(T)$ are presumably more easily evaluated in lQCD than spectral functions; since lQCD is primarily applicable to the finite- T axis, i.e., at $\mu_q=0$, the closest relation to heavy-ion experiments is realized in the central region at RHIC and LHC).
- (3) Perform detailed comparisons of the in-medium effects on the vector correlator with dilepton data (centrality, excitation function, mass and q_t -spectra); this requires additional input from realistic expansion models (e.g. hydrodynamical and transport simulations), which, however, are/can be thoroughly tested against the large body of hadronic observables.

Note that the three different energy-moments of $\rho_V - \rho_A$, as probed by the chiral sum rules, constitute detailed constraints on the energy dependence of the in-medium spectral functions. In addition, each in-medium chiral sum is valid for a given 3-momentum which adds further kinematic information. Therefore, if a chiral hadronic model complies with both theoretical (2) and experimental (3) tests, one has established a tight connection between lattice QCD and data, and therefore deduced explicit evidence for chiral symmetry restoration (without an explicit measurement of the axialvector correlator). In the absence of (unquenched) lattice data for (low-mass) spectral functions for the coming 10 years or so, model approaches are obviously the *only* way to interpret data, and experimental guidance is inevitable to make progress in understanding the underlying nonperturbative physics.

2.7.2. LMR-IMR Transition: Chiral Mixing

In a low-temperature pion gas, the expectation values of vector and axialvector correlators can be evaluated model-independently based on chiral reduction formulae in connection with a low-density expansion. The leading medium effect in the chiral limit has

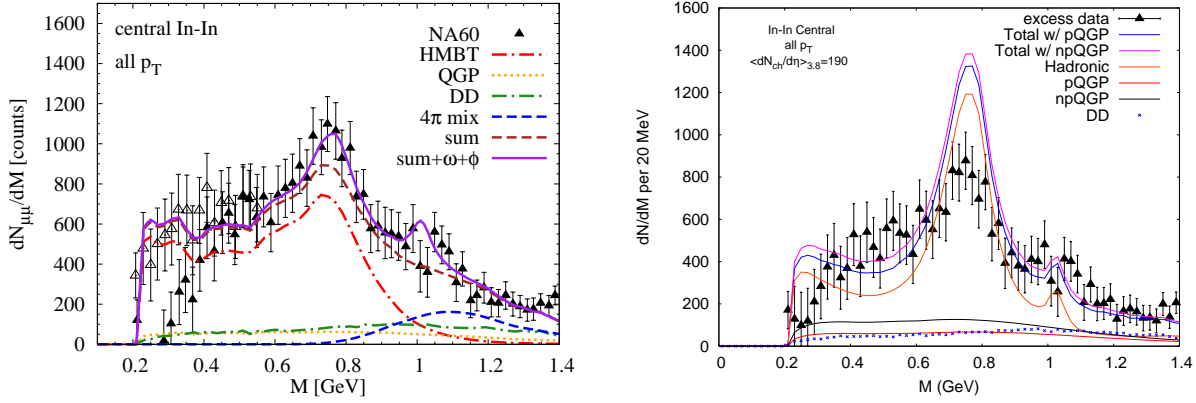


Figure 18. NA60 dimuon data [6, 7] in central In(158 AGeV)+In collisions compared to: (i) left panel: an expanding fireball calculation [107, 108] for QGP and hadronic emission where the latter is based on hadronic in-medium ρ [40], ω [67] and ϕ spectral functions as well as “4 π ” contributions with an enhancement from chiral mixing according to eq. (17); (ii) right panel: hydrodynamic convolution [109] of the dilepton rates following from the chiral virial expansion [88, 98].

first been derived in Ref. [106] and amounts to the so-called chiral correlator mixing,

$$\begin{aligned} \Pi_V(q) &= (1 - \epsilon) \Pi_V^{\text{vac}}(q) + \epsilon \Pi_A^{\text{vac}}(q) \\ \Pi_A(q) &= (1 - \epsilon) \Pi_A^{\text{vac}}(q) + \epsilon \Pi_V^{\text{vac}}(q) , \end{aligned} \quad (17)$$

where $\epsilon = T^2/6f_\pi^2$ encodes the thermal pion density (which is smaller for $m_\pi > 0$). The interactions of the vector current with pions from the heat bath result in a quenching (but do not affected its shape), as well as an admixture of axialvector contributions, induced by $V + \pi \rightarrow A$ and $A + \pi \rightarrow V$ processes, respectively (analogously for the axialvector current). Full mixing corresponds to $\epsilon=1/2$ implying degenerate correlators. While higher-order effects (in both T and ϱ_N) induce a broadening of the ρ resonance (and possibly mass shifts), the mixing leads to the interesting feature of filling the “dip” in the $s=1-2 \text{ GeV}^2$ region of the vacuum vector correlator, cf. left panel of Fig. 17.⁸ A dilepton enhancement in this mass region (by up to a factor of 2 over the vector spectral function on vacuum) is therefore a signature of (the approach to) chiral restoration, via πa_1 annihilation (“4 π ” contributions) which are not present in the vacuum e.m. correlator. Thus far the dilepton data from the SPS did not have the necessary precisions to conduct the required quantitative analysis, recall Fig. 2. It may be feasible with the new NA60 data [6, 7], cf. left panel of Fig. 18. The blue dashed curve represents a theoretical upper estimate [108] by employing eq. (17) with $\epsilon(T) = \frac{1}{2}n_\pi(T)/n_\pi(T_c)$ where $n_\pi(T)$ denotes the pion density at temperature $T \leq T_c$ (including pion chemical potentials below T_c),

⁸In fact, full mixing in this regime leads to (degenerate) V and A correlators that closely coincide with the pQCD $q\bar{q}$ continuum level, which has been interpreted as a lowering of the “duality scale” from $s \simeq 2.5 \text{ GeV}^2$ in the vacuum to about 1 GeV^2 for full mixing. One might go further and interpret the ρ -meson melting as found in hadronic many-body theory (recall Sec. 2.5.1 above) as a lowering of the duality scale for $s \rightarrow 0$, implying chiral restoration [97].

and $T_c=175$ MeV the critical temperature in the evolving fireball. On the one hand, it is gratifying to see that this calculation fully accounts for the excess spectrum in the regime relevant for the mixing; on the other hand, without mixing (not shown) the data are still reasonably well described, illustrating the rather high demand on accuracy in both data and theory (no worse than 20%) to be sensitive to the mixing effect. The chiral virial approach, when folded over a hydrodynamic evolution as shown in the right panel of Fig. 18, also describes the mass region above $M=1$ GeV well [109]; much like in the left panel, a key ingredient is the free e.m. correlator with mixing effects, resulting in an enhancement consistent with the upper and lower limits for maximal mixing and free e.m. correlator. Despite quenching of the ρ peak (recall Sec. 2.5.1), the lack of broadening of the ρ resonance entails a $\sim 40\%$ overestimate of the yield around the free ρ mass; the enhancement below the ρ mass is again accounted for, with important contributions due to baryons. In both approaches underlying Fig. 18, the QGP emission yield is small. Different conclusions have been reached in Ref. [110], where the NA60 data have been fitted with a ρ spectral functions based on pion-gas effects only (cf., however, the comment in Ref. [111]); in addition, the main source of enhancement above the ρ mass has been attributed to QGP radiation.

2.8. Electromagnetic Signatures of the Color Glass Condensate

Although more detailed discussions about Color Glass Condensate (CGC) and related measurements in pA and p+p collisions will be discussed in the “pA and Forward Physics” working group, we include here a section specifically related to the electromagnetic signatures.

Saturation physics has been applied to the description of RHIC data quite successfully, from hadron multiplicities and the phenomenon of limiting fragmentation in $Au+Au$ and $d+Au$ collisions to the produced hadron transverse-momentum spectra in $d+Au$ collisions at mid- and forward rapidity (for recent reviews and an extensive list of references, see Ref. [130]). Nevertheless, in order to establish gluon saturation as the dominant physics responsible for these phenomena at RHIC and beyond, and to rule out various phenomenological scenarios, one needs to consider further tests of the CGC formalism, such as the predictions of saturation physics for electromagnetic processes. In this section we outline electromagnetic signatures of the CGC at RHIC. Specifically, photon and dilepton production in $d+Au$ collisions are considered. These processes have an advantage over hadronic processes in that the produced particles do not interact strongly after they are produced and the non-perturbative process of hadronization is absent. Furthermore, considering photon and dilepton production can shed light on the validity of the recombination model approaches to hadron production which are also capable of fitting the available data, albeit with a few assumptions. *Since saturation physics predicts a similar suppression pattern for photon and dilepton production as for hadron production in $d+Au$, an experimental confirmation of this generic prediction would be a major step in establishing saturation physics at RHIC and in ruling out recombination as the physics of hadron production in $d+Au$ collisions.*

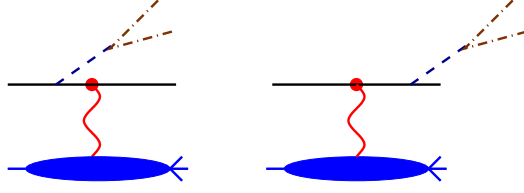


Figure 19. Dilepton production in quark-nucleus scattering.

2.8.1. Dilepton and Photon Production

We consider the dilepton-production cross section in quark-nucleus scattering [131],

$$q(p) + A \rightarrow q(q) + l^+(k_1) + l^-(k_2) + X , \quad (18)$$

shown in Fig.19, where k_1, k_2 are the momenta of the two leptons. Photon production can be obtained by taking the photon virtuality (dilepton invariant-mass) to zero. The differential cross section at fixed impact parameter b_t is given by

$$\begin{aligned} \frac{d\sigma^{qA \rightarrow ql^+l^-X}}{d^2b_t d^2k_t d \ln M^2 dz} &= \frac{2e_q^2 \alpha_{em}^2}{3\pi} \int \frac{d^2q}{(2\pi)^4} \sigma_{dipole}^F(l_t, b_t, x_A) \\ &\left\{ \left[\frac{1 + (1-z)^2}{z} \right] \frac{z^2 l_t^2}{[k_t^2 + M^2(1-z)][(k_t - z l_t)^2 + M^2(1-z)]} \right. \\ &\left. - z(1-z) M^2 \left[\frac{1}{[k_t^2 + M^2(1-z)]} - \frac{1}{[(k_t - z l_t)^2 + M^2(1-z)]} \right]^2 \right\} \quad (19) \end{aligned}$$

where M^2 is the dilepton invariant mass squared with $l_t = q_t + k_t$ and k_t is the transverse momentum of the lepton pair. All quark masses are ignored and z is the fraction of the incoming quark light cone energy carried away by the (virtual) photon while x_A is the Bjorken x probed in the target nucleus.

Eq. (19) is the standard expression one obtains if one assumes the propagation of the incident quark through the nucleus to be eikonal, i.e., the transverse momentum transferred to the nucleus by the incident quark is much less than its longitudinal momentum [132]. All the information on the degrees of the freedom in the target is contained in the dipole cross section $\sigma_{dipole}^F(b_t, l_t, x_A)$. Gluon saturation physics comes in via the dipole cross section which is determined by the evolution equations of the Color Glass Condensate. Given an initial condition for the dipole cross section, the JIMWLK equations in the Color Glass Condensate formalism determine the dependence of the dipole cross section on the collision energy (or alternatively, x_A) and l_t . This is where the main difference between the CGC formalism and the other approaches [132] lies; while the CGC formalism can predict the x_A and l_t dependence of the dipole cross section, other approaches can not and need to motivate a suitable form by phenomenological considerations. We note that, to obtain the invariant cross section for photon production, $\frac{d\sigma^{qA \rightarrow q\gamma X}}{d^2b_t d^2k_t dz}$, from eq. (19), one sets $M = 0$ and takes out the dilepton vertex factor, $\frac{\alpha_{em}}{3\pi M^2}$.

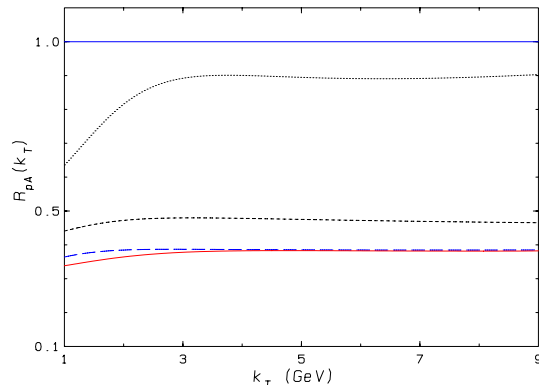


Figure 20. Nuclear modification factor R_{dA} in dilepton production in quark-nucleus scattering. The figure is taken from [133].

Since the dipole cross section is also the main building block figuring into hadron production cross sections in deuteron (proton)-nucleus collisions, one expects a similar behavior for the nuclear suppression factor, R_{dA} , for dilepton production and hadron production. Parametrically, one expects the nuclear modification factor, R_{pA} , to scale with the nucleon number A like $R_{pA} \sim A^{-\frac{\gamma_0}{3}}$ where $1 - \gamma_0 \simeq 0.628$ is the BFKL anomalous dimension. It should be emphasized that in QCD, small- x evolution (BFKL) is the only way to generate leading twist shadowing if one uses partonic degrees of freedom, quarks and gluons.

In case of dilepton production, one has the advantage of having an extra knob to turn, the dilepton invariant mass, in order to change the kinematics and probe the QCD dynamics in different settings. The nuclear suppression factor was calculated in [133] using a saturation inspired model of the dipole cross section and is shown in Fig. 20.

Since the dilepton production rates are small due to the electromagnetic coupling, it is worthwhile to consider the invariant-mass dependence of the cross section, i.e. transverse-momentum integrated cross section. The integration over eq. (19) can be done analytically and the result is given by

$$z \frac{d\sigma^{qA \rightarrow q l^+ l^- X}}{d^2b dM^2 dz} = \frac{\alpha_{em}^2}{3\pi^2} \frac{1-z}{z^2} \int dr_T^2 \sigma_{dipole}^F(x_g, \underline{b}, r_T) \left[[1 + (1-z)^2] K_1^2 \left[\frac{\sqrt{1-z}}{z} M r_T \right] + 2(1-z) K_0^2 \left[\frac{\sqrt{1-z}}{z} M r_T \right] \right]. \quad (20)$$

To relate this to proton (deuteron)-nucleus scattering, we need to convolute eq. (20) with the quark (and anti-quark) distributions $q(x, M^2)$ in a proton (deuteron). As shown in [132], this can be written in terms of the proton (deuteron) structure function F_2 ,

$$\frac{d\sigma^{pA \rightarrow l^+ l^- X}}{d^2b dM^2 dx_F} = \frac{\alpha_{em}^2}{6\pi^2} \frac{1}{x_q + x_g} \int_{x_q}^1 dz \int dr_T^2 \frac{1-z}{z^2} F_2^p(x_q/z) \sigma_{dipole}^F(x_g, \underline{b}, r_T)$$

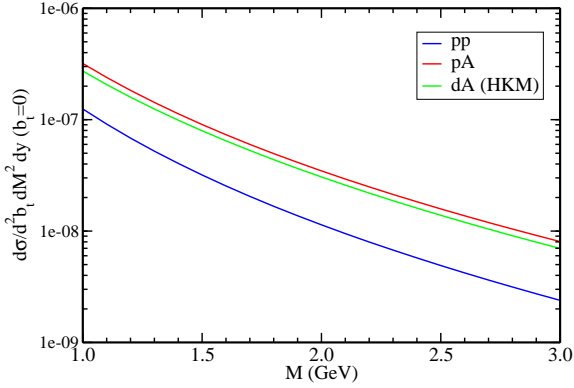


Figure 21. Invariant cross section for dilepton production at $y = 2.2$.

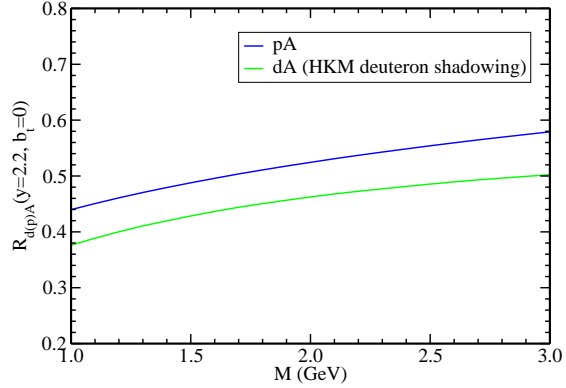


Figure 22. Nuclear modification factor for dilepton production at $y = 2.2$.

$$\left[[1 + (1 - z)^2] K_1^2 \left[\frac{\sqrt{1 - z}}{z} M r_T \right] + 2(1 - z) K_0^2 \left[\frac{\sqrt{1 - z}}{z} M r_T \right] \right] \quad (21)$$

where

$$\begin{aligned} x_q &= \frac{1}{2} \left[\sqrt{x_F^2 + 4 \frac{M^2}{s}} + x_F \right] \\ x_g &= \frac{1}{2} \left[\sqrt{x_F^2 + 4 \frac{M^2}{s}} - x_F \right] \end{aligned} \quad (22)$$

with $x_F \equiv \frac{M}{\sqrt{s}} [e^y - e^{-y}]$, and

$$F_2^p \equiv \sum_f x [q_f(x, M^2) + \bar{q}_f(x, M^2)]$$

is the proton structure function.

In Fig. 21 we show the invariant cross section for dilepton production in proton-proton, proton-nucleus and deuteron-nucleus collisions as a function of dilepton invariant-mass while in the Fig. 22 we show the nuclear modification factor for both proton-nucleus and deuteron-nucleus collisions at RHIC. In both cases, the rapidity is $y = 2.2$ and the results are for the most central collisions [134]. In case of a deuteron projectile, the HKM parameterization of the deuteron wave function is used (which leads to a few-percent effect).

Using the same formalism, photon production as well as photon and hadron correlation function have been calculated [134]. It has been shown that the hadron-photon cross section is a very sensitive probe of the dipole profile which is the main ingredient of single-particle production cross section in the CGC formalism. Therefore, experimental studies of electromagnetic probes such as photons and dileptons in deuteron-nucleus collisions at RHIC can shed light on the dynamics of gluon saturation and whether the observed suppression of the hadron spectra in the forward rapidity region at RHIC is due to saturation physics. This measurement will also be able to clarify the role of hadron recombination

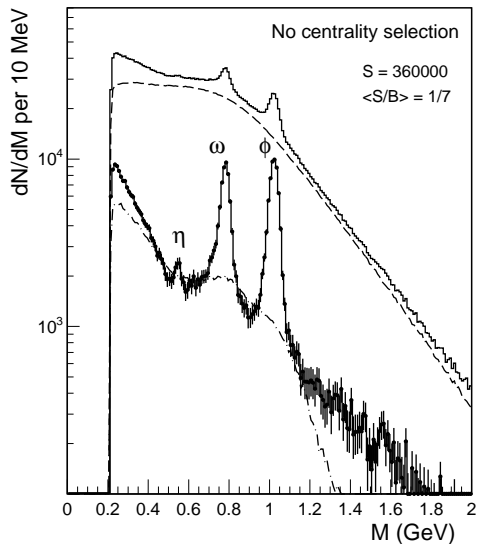


Figure 23. Dimuon invariant-mass spectra from NA60 [6, 7]. The raw data (upper histogram) show clear ω and ϕ peaks. In the background-subtracted spectrum (lower histogram) even the $\eta \rightarrow \mu\mu$ decay is well recognizable.

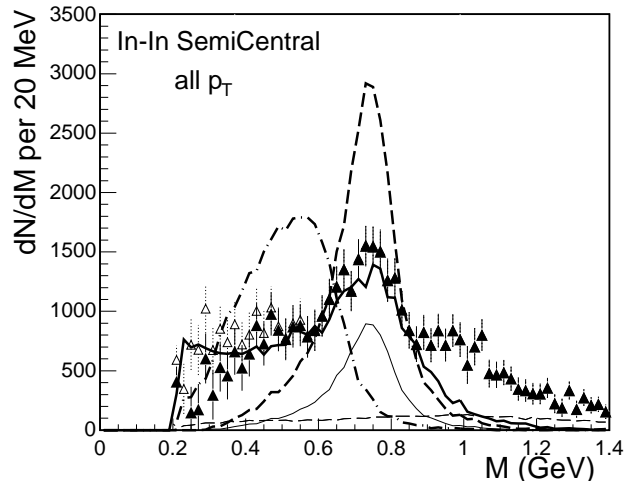


Figure 24. Excess dimuon-mass spectrum from NA60 [6, 7], compared to predictions of various theoretical scenarios (vacuum ρ (dashed line), dropping mass [42] (dash-dotted line) and hadronic many-body [40]). The spectral functions and expanding fireball model are the same as used in the upper panel of Fig. 2 in connection with the CERES data. Much increased experimental precision can now distinguish in-medium scenarios.

models at RHIC, at least in the forward rapidity region since recombination effects will not be present in electromagnetic processes and therefore an observed suppression of the dilepton or photon nuclear modification factor will be strong evidence for the CGC.

It is worth noting that, since the saturation scale of the proton (deuteron) is very small at mid- or forward rapidity at RHIC, CGC predictions for proton-proton collisions will have large uncertainties. As a matter of fact, as shown very recently [135], one can not reliably calculate particle production in proton-proton collisions at RHIC while $d+Au$ collisions are under much better quantitative control. Therefore, in any saturation-inspired calculation of the nuclear modification factor, the denominator (p - p cross section) should be understood as a fit to the data while the $d+Au$ cross section can be calculated using saturation physics and can be used to confirm/rule out the latter as the dominant physics in the forward-rapidity region at RHIC. This, in turn, will have significant ramifications for LHC.

3. OBSERVABLES: STATE OF THE ART

3.1. Low-Mass Dileptons

The ρ meson with its short lifetime (1.3 fm/ c in vacuum), large dilepton decay width ($\Gamma_{ee} = 7$ keV) and prevalent coupling to $\pi\pi$ (and possibly $q\bar{q}$) annihilation has long been

identified as the most promising probe for in-medium modifications of hadron properties close to the QGP phase boundary: changes in its width and/or mass were anticipated as precursors of the chiral transition more than two decades ago [136]. Dielectron mass spectra from CERES [33, 47] over the last ten years have shown a significant (factor of 2-3) excess over known hadronic sources in the mass region below the free ρ mass – a result which spurred vigorous theoretical activity, but experimental uncertainties (including limited statistics and mass resolution) of the CERES data did not allow to either confirm or refute the suggested scenarios with medium effects⁹. Recently the NA60 experiment at SPS (a significant *upgrade* of NA50, adding among others high-precision tracking close to the vertex in a high magnetic field) measured dimuon-mass spectra in 158 AGeV $In+In$ collisions with an unprecedented ~ 20 MeV mass resolution and statistics in both LMR and IMR [6, 7]. The results in the light vector-meson region are shown on Fig. 23. After subtracting the “hadron decay cocktail” (η , ω , ϕ) the excess spectrum has a clear albeit rather broad peak around the nominal ρ mass, as shown on Fig. 24 and compared to theoretical predictions using in-medium ρ spectral functions with either a dropping mass [42] or a strong broadening as calculated in hadronic many-body theory [40]. The excellent resolution and statistics, *made possible by detector upgrades and high luminosity*, now clearly enables to distinguish between these two approaches - and can be considered as a benchmark for future dilepton measurements (in how far other approaches can postdict the data remains to be seen). Such precision measurements - rendered possible by RHIC-II - will be essential to further improve our understanding and elevate it from the qualitative to the quantitative level, which is necessary to draw any conclusions about the nature of chiral symmetry restoration.

Measurements of the ρ spectral function of comparable quality do not yet exist at RHIC, but STAR found indications from $\pi^+\pi^-$ invariant-mass spectra [114] that the ρ mass is both p_T and multiplicity-dependent in $p+p$, $d+Au$ and peripheral $Au+Au$ collisions. At low transverse momenta ($\sim 0.5 - 1.5$ GeV/c) the peak position moves down by 3-8%, but whether this is caused by a ρ -mass shift [116, 117] or other effects (e.g., Bose-Einstein correlations, thermal phase space in connection with a broadening, underlying “ σ ”-decays, etc. [113, 118]) remains to be clarified. The measurement did not have sensitivity to study possible changes in the ρ width [115], which again requires an improved determination of the background sources (including “physics background”).

We should also point out that the combination of leptonic ($\rho \rightarrow ee$, probing the entire collision history, at least in the hadronic phase) and hadronic ($\rho \rightarrow \pi\pi$, probing the late/surface regimes of the fireball) decay channels of the ρ is a valuable tool to disentangle in-medium modifications of the hot and dense phases from the more dilute ones.

3.2. The $\phi(1020)$: Hadronic vs. Leptonic Decays and v_2

Since the ϕ mass is barely above twice the kaon mass ($m_\phi - 2m_K \simeq 30$ MeV), a study of hadronic $\phi \rightarrow KK$ vs. leptonic $\phi \rightarrow ee$ decays has long been suggested as a sensitive test to a dropping (or broadening) of the ϕ mass (width), possibly related to (partial) chiral symmetry restoration. If the mass drops, the (dominant) $\phi \rightarrow KK$ decay quickly becomes kinematically suppressed, and the ratio of production cross sections, $\sigma(\phi \rightarrow KK)/\sigma(\phi \rightarrow$

⁹A significant improvement in mass resolution has been achieved with the Time-Projection-Chamber upgrade of the CERES detector [137].

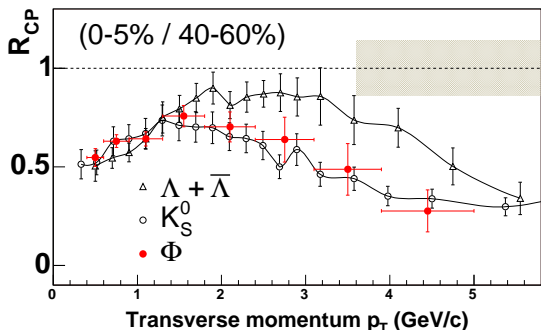


Figure 25. Nuclear modification factor R_{CP} (ratio of yields in central and peripheral collisions, divided by the respective number of binary $N-N$ collisions) for ϕ , K_s^0 and Λ in 200 GeV $Au+Au$ [140].

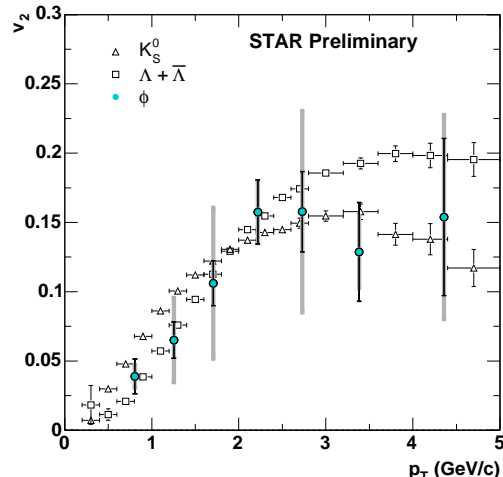


Figure 26. Elliptic flow as a function of p_T for ϕ , K_s^0 and Λ in 200 GeV $Au+Au$ [140].

ee), in the hadronic (branching ratio $BR=49.2\%$) and leptonic ($BR=3*10^{-4}$) should change dramatically (similar arguments may apply if a reduction in kaon masses, or inelastic reactions such as $\phi + \pi \rightarrow K + K^*$, lead to strong increase of the ϕ width; in this case, the effects of ϕ regeneration have to be accounted for as well) [138]. Recent preliminary results from PHENIX [139] suggest that $dN/dy(\phi \rightarrow ee)$ is larger, and that the m_t slopes are steeper, in A-A compared to $p-p$ collisions - but the experimental errors prevent from reaching definite conclusions. Once again, the main problem is the small signal-to-background ratio (S/B) in the dielectron channel, *to be cured only with better background rejection*. On the other hand, ϕ yields from $\phi \rightarrow KK$ extracted from STAR's measurements [140] are systematically higher than those measured by PHENIX in the same decay channel, although a careful analysis shows that the data points in the p_T spectra are not inconsistent between the two experiments [141]. We note that there is a difference between $\phi \rightarrow KK$ measured by NA49 and $\phi \rightarrow ee$ measured by NA50. Recent CERES [142] (NA60 [143]) results on $\phi \rightarrow KK$ and $\phi \rightarrow ee$ in $Pb+Au$ ($\phi \rightarrow \mu\mu$ in $In+In$) collisions are consistent with those from NA49. One thus concludes that the difference is not due to the different decay channels under study. These findings reiterate the importance of powerful detector upgrades and the ability to measure different decay channels in large momentum coverage and in the same apparatus.

Since the ϕ is a meson but with a mass comparable to baryons, it also plays a major role in distinguishing between mass- and particle-species dependence of quantities like the nuclear modification factor, R_{CP} , and elliptic flow. Recent results from STAR [140] in 200 GeV $Au+Au$ collisions show that both R_{CP} (Fig. 25) and v_2 (Fig. 26) are consistent

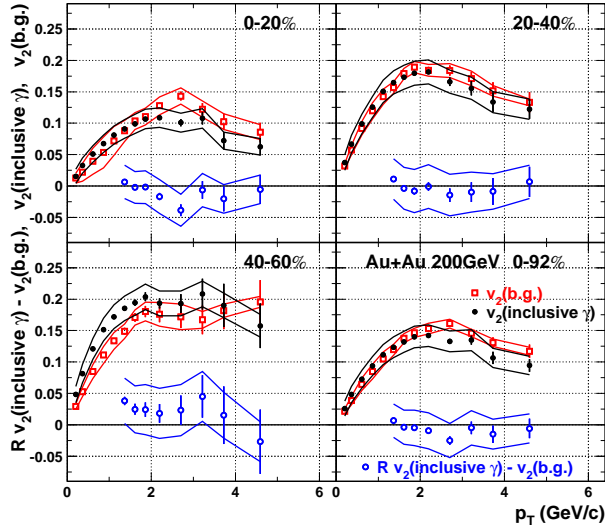


Figure 27. The measured v_2 of inclusive photons ($v_2^{\text{inclusive } \gamma}$, solid circles) and expected photon v_2 from hadronic decays ($v_2^{\text{b.g.}}$, open squares) [144]. A subtracted v_2 quantity $R v_2^{\text{inclusive } \gamma} - v_2^{\text{b.g.}}$ is plotted at the bottom of each panel (open circles), where $R = (N_{\text{direct } \gamma} + N_{\text{b.g.}})/N_{\text{b.g.}}$ corresponds to a product of the direct photon v_2 and a positive factor $R - 1$, ($v_2^{\text{direct } \gamma}(R - 1)$). The different panels are for the different centralities.

with parton recombination and collective flow at the partonic level.

3.3. Photon Azimuthal Asymmetries (Elliptic Flow)

We have seen in Fig. 1 that the *overall* yields of high- p_T photons (integrated over azimuth) scale with N_{coll} and are well described by pQCD (within current experimental and theoretical uncertainties). However, this global agreement may mask more subtle effects and it is even possible that the agreement is only accidental, due to cancellations of processes that enhance and others that quench the photon yield. An important step toward clarification is to study azimuthal asymmetries of photon distributions, specifically their elliptic flow (v_2). If (and since) the photons from the initial scattering do not interact with the medium, their v_2 is expected to be zero. However, photons in A+A collisions are not only produced in the initial hard scattering. On the one hand, they may also originate from jet partons scattering off thermal partons (jet-thermal interactions) or from Brehmsstrahlung off a quark. These photons are expected to exhibit a negative v_2 [10, 11], since more material is traversed out-of-plane (which is the major axis in coordinate space), with a strong p_T -dependence. On the other hand, photons from thermal radiation should reflect the dynamical evolution of the hot and dense matter thus carrying a positive v_2 .

A first measurement of photon elliptic flow is shown in Fig. 27 taken from Ref. [144]. The measurement is quite delicate due to the large background from π^0 decay-photons that inherit their parent's v_2 . The measured v_2 of inclusive photons is consistent with v_2 of photons from hadronic decays, i.e., a zero net direct photon flow - but the error

bars are appreciable and the direct-to-inclusive photon ratio is very small at low p_T . The quality of the data currently available is not sufficient to prove or disprove theoretical predictions [10, 11], not even the sign of the net flow. Much higher statistics can help remedy the situation, at least at higher p_T : although the net direct photon flow is predicted to decrease, the statistical errors will also become smaller and, equally important, the direct-to-inclusive photon ratio increases dramatically. But even at high p_T the net flow will be a competition between processes with $v_2 > 0$ and $v_2 < 0$. New analysis techniques may be able to disentangle (at least statistically) isolated and non-isolated direct photons in heavy-ion collisions. Jet-photon conversions produce mostly isolated photons [10] with $v_2 < 0$ and the magnitude of this flow depends strongly both on p_T and the energy-loss mechanism of jets in heavy-ion collisions. Therefore, a measurement of the v_2 for isolated photons may give an independent constraint on energy-loss models.

3.4. Electron R_{AA} and Flow

The recent measurement of “non-photonic” single-electron spectra (i.e., those associated with decays of open heavy-flavor hadrons) at RHIC lead to two unexpected and very important results: (i) the nuclear modification factor, R_{AA} , shows a strong suppression in central $Au+Au$ collisions [152, 153], comparable to the suppression observed for pions; (ii) the elliptic flow, v_2 , at low p_T is significant, up to 10%. The strong suppression is a surprise because heavy quarks were expected to lose much less energy than light quarks, and the strong flow at low p_T indicates substantial (early) collectivity of (at least the) charm. These issues concern primarily charm and bottom physics, and are discussed in detail in the write-up of the Heavy-Flavor Physics Working Group. However, they have significant relevance to the “classic” electromagnetic probes, since the suppression of charm (and bottom?) actually *helps* the measurements of continuum dilepton (QGP?!) radiation at intermediate masses, by reducing the combinatorial background from charm (irreducible in case of the PHENIX HBD) in this regime (see Fig. 30).

3.5. Direct Photons via Low-Mass Dielectrons

A very promising approach to measure low- p_T direct photons is to utilize low-mass electron pairs from “internal conversions”, as has been first applied in heavy-ion collisions recently by PHENIX [70]. The basic idea is that any process producing a real photon can also produce a virtual one of very low mass [155], subsequently decaying into an e^+e^- pair. This direct photon signal competes, of course, with dielectrons from Dalitz decays of π^0 , η , etc . The rate and mass distributions of dielectrons are described both for the low-mass direct photons and the Dalitz decays by the Kroll-Wada formula [155],

$$\frac{1}{N} \frac{dN_{ee}}{dm_{ee}} = \frac{2\alpha}{3\pi} \sqrt{1 - \frac{4m_e^2}{m_{ee}^2}} \left(1 + \frac{2m_e^2}{m_{ee}^2}\right) \frac{1}{m_{ee}} |F(m_{ee}^2)|^2 \left(1 - \frac{m_{ee}^2}{M^2}\right)^3, \quad (23)$$

where the form factor, F , is unity for real photons. Note that the phase space for Dalitz decays is limited by the mass of the parent meson ($m_{ee} < M_{\pi^0, \eta, \omega}$), while for direct photons it is not ($m_{ee} \sim p_T$). Therefore, the measurement becomes relatively clean for $p_T > 1$ GeV/c, which is still in the low- p_T realm where the “traditional” calorimeter measurement has serious difficulties. The method is illustrated in the left panel of Fig. 28, and the resulting photon excess ratios are shown in the right panel. The systematic

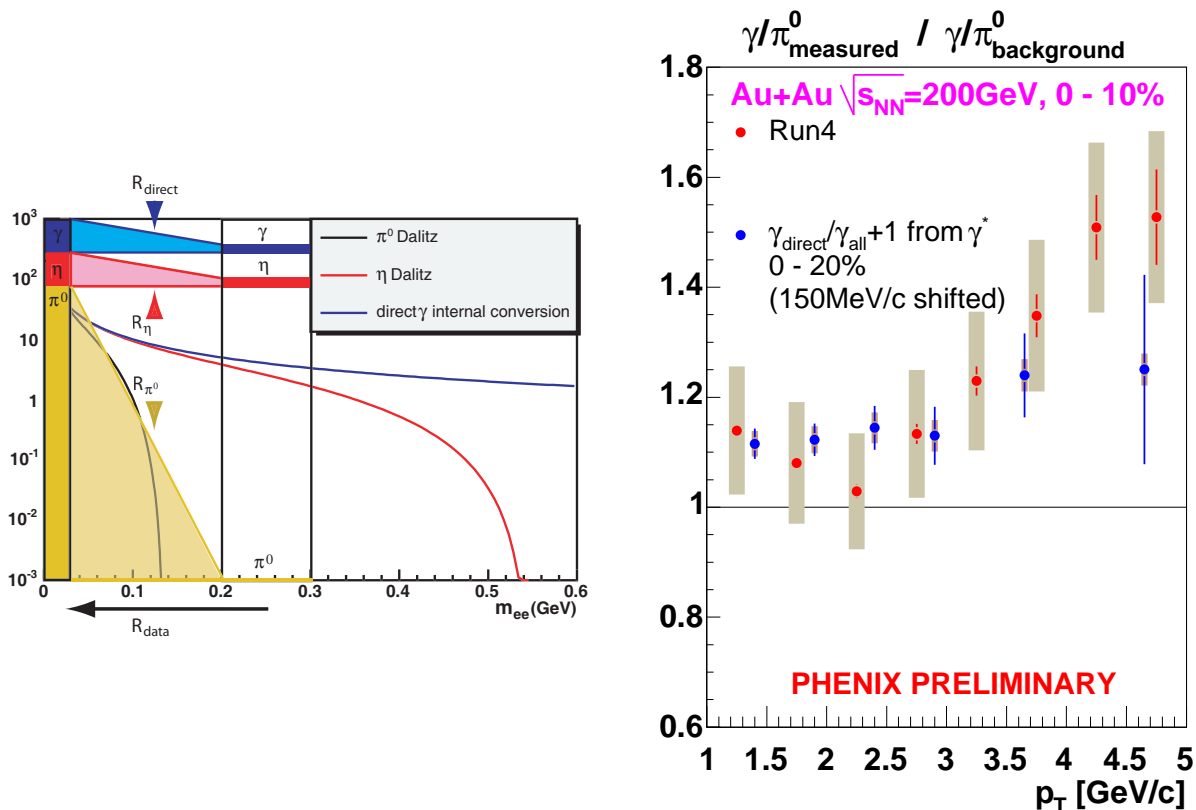


Figure 28. Left panel: illustration of the direct photon measurement via low-mass dileptons [70]. Right panel: latest results on low- and intermediate- p_T direct photons (given as the “photon excess ratio”) with the traditional calorimeter method (red circles) and via low-mass electron pairs (blue circles).

errors are much smaller for the new method¹⁰, but the statistical errors become large for $p_T > 4 \text{ GeV}/c$, albeit ~ 15 times more data have been analyzed for dielectrons (solid red circles) than in the displayed calorimeter analysis (open blue circles). We believe that there is an important lesson here: even for signals like thermal photon radiation, which is typically not considered to be “starving for statistics”, novel but *very promising new analysis techniques require a large increase in luminosity*.

The conversion approach is also appealing from the theoretical point of view, since the framework outlined in Sect. 2.1 accommodates a comprehensive treatment of real and virtual photons, as represented by eqs. (1) and (2). However, more theoretical work is needed for a more complete assessment of possible sources of very-low mass dielectrons [46].

¹⁰At least on the direct photon excess *ratio*; however, the absolute normalization and the direct photon cross section are difficult to assess, and therefore have been inferred in the “traditional way” with the calorimeter.

4. THE FUTURE

4.1. Detector upgrades

Already in their original design both PHENIX and STAR anticipated later upgrades to enhance the physics capabilities of the detectors. In fact “upgrading” as a response to spectacular rises in luminosity and physics insights from data already taken was and remains an almost continuous process from the very start of operations and few can be tied uniquely to RHIC-II (with the exception of upgrades facilitating the handling of high luminosities and data rates). Nonetheless, several major projects should be discussed in our context both because of their magnitude and their impact on future capabilities at RHIC-II (see Table 1). They are at different degrees of development: some are in the early R&D phase, others will already be installed within months (for Run-7). Here we will concentrate on those upgrades that are particularly important for studying electromagnetic probes. The STAR Time-of-Flight (TOF) detector and Heavy Flavor Tracker (HFT) improve the electron identification and displaced vertex measurement (rejection of electrons from charm, bottom and Dalitz decays as well as conversion electrons). The PHENIX Hadron Blind Detector (HBD) will reject Dalitz pairs for the measurement of light vector mesons, the Silicon Vertex Detector (SVTX) will measure displaced vertices to identify electrons from open charm. A new high-resolution sampling calorimeter is proposed for STAR to measure direct photon correlations. In the following, we will elaborate on these systems in more detail.

4.1.1. STAR Time-of-Flight and Heavy Flavor Tracker

At STAR electron identification is made possible by a combination of a measurement of the energy loss by charged particles due to ionization (dE/dx) of the time-projection-chamber (TPC) gas and a velocity measurement with the TOF system [156]. The relativistic rise of the electron dE/dx separates electrons from hadrons except at the crossovers with pions at momentum of $\sim 0.2\text{GeV}/c$, with kaons at $\sim 0.6\text{GeV}/c$, with protons at $\sim 1.1\text{GeV}/c$ and with deuterons at $\sim 1.5\text{GeV}/c$. A time-of-flight measurement, with the requirement that $|1 - \beta| < 0.03$, eliminates slow hadrons and cleans up the crossovers. This results in clean electron identification [156].

In addition to direct measurements of open-charm hadrons (via $K\pi$ decays), the STAR HFT [157] will serve as a powerful device to discriminate primordial electrons from background electrons in the measurement of electromagnetic probes.

As discussed earlier, direct production of photons and leptons is rare and overwhelmed by photons and leptons from electromagnetic decays of hadrons with subsequent γ conversions to electrons ($\gamma \rightarrow e^+e^-$). The latter are, to a large extent, due to conversions in the detector material. The HFT detector will reduce the background electrons and positrons from these γ conversions. By requiring hits in the HFT, electrons from photon conversion outside the HFT, i.e., in the Silicon Strip Detector (SSD, the upgraded STAR Silicon Vertex Tracker) and the TPC inner field cage, are rejected. To estimate the signal-to-background ratio in the vector-meson measurements, we adopt a reasonably conservative approach and assume that the HFT can reject γ conversions by a factor of 10 [157]. Another source of electron background arises from semileptonic decays of heavy quarks, charm (c) and bottom (b). If heavy-quark spectra are extrapolated from p - p collisions, the dominant dilepton source in central $Au+Au$ at intermediate mass [69]

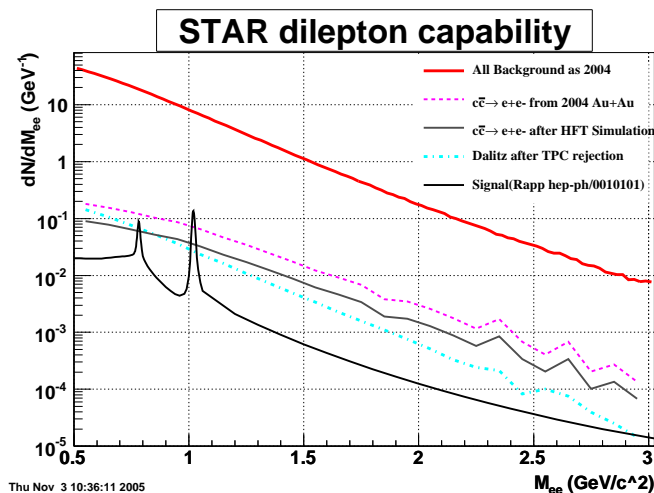


Figure 29. Dielectron invariant mass distributions for central 200 GeV $Au+Au$ collisions. The solid black curve is the prediction for thermal emission of Ref. [69] with STAR acceptance. The red curve at the top is the total di-electron invariant-mass spectrum with year-2004 configuration assuming electron PID from full TOF coverage. The pink dashed line is the e^+e^- pair spectrum from semileptonic charm decays, the grey curve the charm e^+e^- spectrum after HFT $DCA < 80 \mu m$, and the dot-dashed line are from Dalitz decays of π^0 and η after rejection from the TPC.

is due to semileptonic $c\bar{c}$ decays. With the large charm yield at RHIC energy, the latter are comparable to the yield from γ conversions and Dalitz decays of π and η after the HFT rejection described above. Detailed simulations show that the HFT is capable of rejecting $\sim 75\%$ of e^+e^- pairs from the D^0 decay while preserving 50% of the direct e^+e^- pairs.

The large reduction in electron background will enable us to observe the electromagnetic signal from low-mass vector mesons and radiation of intermediate-mass dileptons with a few hundred thousand central $Au+Au$ events in STAR. The rejection of π^0 and η Dalitz decays by a factor of 3 (single track) can be achieved by measuring both electrons of the pair which is possible due to the large acceptance of the STAR TPC. With the upgrades we expect to detect 6K ϕ and 22K ω decays in 200 million recorded central $Au+Au$ collisions. These are to be compared with the numbers presented by NA60 at QM05 [143] in central $In+In$ collisions: $\sim 6K$ for the ω and $\sim 10K$ for the ϕ .

Fig. 29 summarizes the dielectron invariant-mass distributions of background and signals. The signals of medium-modified vector mesons and thermal QGP radiation (black curve) are from calculations of Ref. [69] folded over the STAR acceptance. The uppermost (red) curve is the total dielectron invariant-mass spectrum with year 2004 configuration. This is obtained from the single-inclusive electron spectrum measured in 200 GeV $Au+Au$ collisions with the assumption of electron PID from full TOF coverage. The pink dashed line is the e^+e^- pair spectrum from semileptonic charm decays derived from the non-photon single-electron spectra measured in $Au+Au$ collisions. The gray curve is

the charm e^+e^- distribution after applying the HFT distance of closest approach cut, $DCA < 80 \mu\text{m}$. The dot-dashed line is from Dalitz decays from π^0 and η in the TPC after rejection. The net results is a signal-to-background ratio that, even in the continuum regimes, is around (or better) than 1/10, which is very comparable to the NA60 measurements for central $In+In$ [7]. The standard method of dealing with the residual background is by mixed-event methods. This has been used by CERES and NA50/NA60 at the SPS and will be used both in PHENIX and STAR.

Let us now turn to the data-taking and luminosity requirements for dileptons in STAR. With the proposed upgrades of Time-of-Flight, Heavy-Flavor Tracker and Data Acquisition System (DAQ1000), STAR will be able to take data at a rate of 1000 Hz with very little dead time; at the same time, the collision vertex has to be limited to $\sim \pm 5$ cm due to the acceptance of the HFT [157]. These are to be compared to a current data-taking rate of 50 Hz and a collision diamond of $\sim \pm 50$ cm. Without machine upgrade, the average luminosity delivered to STAR is $8 \times 10^{26} \text{cm}^{-2}\text{s}^{-1}$ or 6 kHz of $Au+Au$ minbias nucleus collision rate. Taking into account the vertex constraint (factor of 3-5 loss) and centrality binning in $Au+Au$ events (e.g., 10% most central), central-triggered $Au+Au$ events can be recorded at a rate of about 200 Hz with all the available luminosity, significantly below the DAQ1000 capability. A factor of 10 luminosity upgrade will enhance both the collider and detector into their full capability. In addition, for peripheral collisions, the statistics will be lower due to lower multiplicities per event. However, triggering will be more effective even for low- p_T lepton pairs. Since the luminosity decreases quadratically with decreasing beam energy, an efficient energy scan at RHIC definitely requires a luminosity upgrade, as discussed in more detail in Sect. 4.3 below.

4.1.2. PHENIX Hadron Blind Detector and Silicon Vertex Detector

As discussed earlier, the measurement of the low-mass (electron) pair continuum to infer the in-medium modifications of the light vector-meson (ρ , ω , ϕ) spectral functions is crucial to understand the fate of hadronic masses and (the approach to) chiral symmetry restoration in the hot dense matter created in heavy-ion collisions. However, the e^+e^- signal is overwhelmed by the combinatorics from π^0 Dalitz decays and photon conversions; combinatorial background from open-charm decays is also significant (see Fig. 30). Fortunately, both for π^0 Dalitz and photon conversions the typical opening angle of the e^+e^- pair is very small, so unless they are swept apart by a magnetic field a proximity cut on electron pairs is an effective veto on Dalitz and conversion electrons. The PHENIX magnet has an inner and an outer coil which typically are powered by currents in the same direction (for maximum field to optimize tracking to the highest possible p_T). However, the current in the inner coil can be reversed making the magnetic field vanishingly small around the collision region which allows the installation of a ‘‘Hadron Blind Detector’’ (HBD) to eliminate the combinatorial background from Dalitz and conversions. This detector (described in Ref. [158]) is a windowless Cherenkov detector operated with pure CF_4 in proximity focus configuration with a CsI photocathode and a triple GEM detector with pad readout. It is a crucial upgrade for the exploration of the properties of the new matter created. As illustrated in Fig. 30 it will reduce the combinatorial background and increase the signal/background ratio from $\sim 10^{-3}$ to $\sim 10^{-1}$. The latter is again very comparable to NA60 and the expected performance of STAR after upgrades (cf. previous

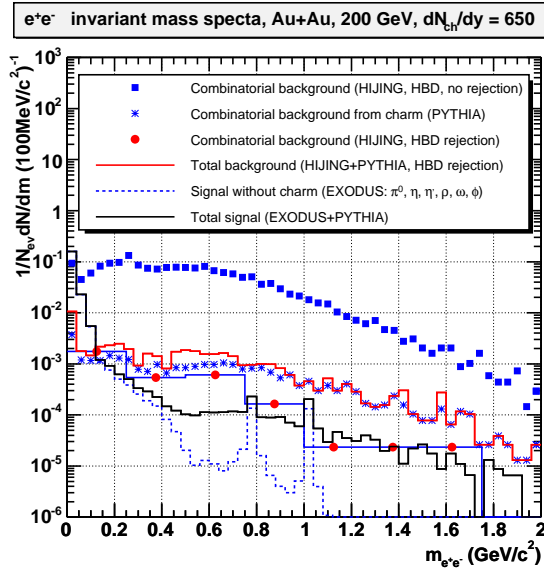


Figure 30. Combinatorial background for low-mass electron pairs compared to the total signal from vector mesons and charm with and without the HBD. Blue squares: total e^+e^- combinatorial (HIJING), no rejection from the HBD. Red circles: combinatorial background after rejection with HBD. Blue stars: combinatorial background from charm alone (PYTHIA), not rejected by the HBD, measured separately by the Silicon Vertex Detector (SVTX). Solid red line: total combinatorial background after HBD rejection (HIJING+PYTHIA). Dashed blue line: pure signal from direct vector-meson and Dalitz decays after freezeout (“cocktail”), without contribution from charm (EXODUS). Solid black line: total signal from vector mesons, Dalitz decays and charm (EXODUS+PYTHIA).

section).

The remaining background from open charm will be measured in PHENIX separately with a Silicon Vertex Detector (SVTX), which will measure the heavy-flavor displaced vertex with a $40\mu\text{m}$ resolution of the distance of closest approach, the specification driven by $c\tau$ of 123 and $462\mu\text{m}$ for D^0 and B^0 decays, respectively. The SVTX will have a central barrel and two endcap detectors, thus covering both central and forward rapidities, providing inner tracking with full azimuthal coverage and up to $|\eta| < 2.4$. This, in particular, will enable the measurement of correlated $e\mu$ invariant-mass spectra and thus provide for a stand-alone determination of the correlated open-charm (and -bottom) component in the dilepton spectra.

4.1.3. The PHENIX Nose-Cone Calorimeter

Photons, π^0 and η mesons can be measured well at mid-rapidity in PHENIX, but the y -coverage of the electromagnetic calorimeter (along with the current “central arm”) is limited to $|y| < 0.35$. This makes full jet reconstruction very difficult. Also, several measurements made at large rapidities in $d+Au$ collisions suggest that in the low Bjorken- x domain gluons might be saturated and the CGC-model properly describes the results,

including hadron suppression at large rapidities in $d+Au$ (as opposed to no suppression as observed at $y = 0$). If the suppression at large y is indeed a consequence of gluon saturation (initial state), photons should also be suppressed there (cf. Sec. 2.8) - an important test feasible only with a calorimeter at large rapidities. The limited acceptance of the central arm also makes the crucial γ -jet measurements very difficult.

To remedy the situation PHENIX proposed to add a calorimeter replacing the current copper nosecones of the magnet and covering $1 < |\eta| < 3$. This “Nose-Cone Calorimeter” (NCC) is a silicon-tungsten sandwich sampling calorimeter, longitudinally segmented in 3 sections and read out by $1.5 \times 1.5 \text{ cm}^2$ Si pads. In addition, at 2 and 7 radiation lengths two layers of $468 \mu\text{m}$ pitch strip-pixels are added to achieve separation of direct photons from high-energy π^0 s by shower shape reconstruction. The total depth is $\sim 42X_0$ radiation and $1.6L_{abs}$ nuclear absorption length, the expected resolution for electromagnetic showers is $14\%/\sqrt{E}$. The longitudinal segmentation allows for distinction between electromagnetic and hadronic showers, and the coverage is sufficient to reconstruct the entire jet energy.

Therefore, jet physics and energy-loss studies using both photon-tagged jets and leading π^0 's will be possible with the NCC, far away from central rapidity. It will also be very useful in studying heavy quarkonia enabling for instance the measurement of $\chi_c \rightarrow \gamma J/\psi$ and possibly the $\chi_b \rightarrow \gamma \Upsilon$ states in conjunction with the existing muon spectrometer, thus giving information on the different quarkonium dissociation temperatures (and feed-down contributions to the J/ψ yields) [159, 160]. The NCC is also an important addition to the spin program in measuring the (polarized) gluon structure functions at low x .

4.2. New Measurements

4.2.1. Direct Photon Correlations (HBT)

The HBT correlation of photons from a π^0 (or η) decay is exceedingly small because of the “large” distance of $> 10^7 \text{ fm}$ at which the decay occurs. Typical correlations from π^0 decay photons are $\mu\text{eV}/c$ in relative four-momentum between the photons. Therefore, any measurable HBT correlation will come from photons directly emitted from the collision.

Photon HBT correlations encode information about the space-time properties of the system which emits the direct photons. Many calculations, as well as “simple” quantum mechanics, indicate that by looking at the HBT for different regions of p_T , one can identify emitting systems of different temperatures and hence at different stages of evolution of the collision system [162]. In addition, interferometry can also be used to measure the yield of direct photons [39].

The effect of the π^0 decay background is to *dilute* the HBT signal, but the decay in itself does not generate a fake correlation. However, the residual correlation of decay photons due to the HBT correlations of the π^0 mesons themselves *could* cause a fake HBT correlation. It has been found that when the measured HBT parameters as determined from charged pions are added into a Monte Carlo calculation of the residual correlation, the change is negligible compared to reasonable estimates of the direct photon correlation (assuming, of course, that the HBT parameters for the π^0 are the same as for charged pions) [161].

The aforementioned dilution effect, on the other hand, is a serious issue. Reasonable estimates of the visible HBT correlation indicate that λ , the effective amplitude of the HBT correlation, is only a few parts per thousand. Consequently, great care must be

used in designing experiments to measure the direct photon HBT. Corresponding work on this problem is briefly summarized in the remainder of this section, based on a more complete, technical paper that is under preparation [161].

Within the context of the STAR detector it has been found that the best way to measure the HBT correlation is to use one photon that converted to an e^+e^- pair in a thin (10% X_0) converter placed inside the inner-field cage of the TPC and another (real) photon detected in the barrel calorimeter. This way one can be sensitive to photons whose directions are very close, even identical. However, it has been found that in order to make useful measurements of the HBT radius parameters, the energy resolution of the electromagnetic calorimeter must be substantially improved over the resolution of the present calorimeter ($\delta E/E = .15/\sqrt{E}$). Pertinent studies show that $\delta E/E = .03/\sqrt{E}$ is certainly sufficient and some preliminary Monte Carlo data indicate that even $.05/\sqrt{E}$ may be adequate, although near the “limit”. Currently work is in progress to determine the precise requirements, along with studies of recent progress on the “shashlyk” design, a relatively cheap calorimeter where alternating plates of radiator and scintillator are read out by an array of wavelength shifting fibers which run parallel to the long axis of the calorimeter and penetrate the radiators and the scintillators. The technology is well established: a shashlyk calorimeter used in E-865 at the AGS achieved $.08/\sqrt{E}$ resolution, and 3/4 of the PHENIX calorimeter was built (ten years ago) to a similar design and shows similar performance. Subsequent studies done for the KOPIO experiment have demonstrated that even $.03/\sqrt{E}$ resolution is achievable. The designers of this calorimeter are now engaged in a design study of a shashlyk calorimeter that could be used in STAR.

In subsequent feasibility studies, a model of direct photon production has been constructed which agrees with both existing measurements at $p_t \geq 2.0$ GeV/c and a recent calculation below that value [18]. The model assumes Bjorken (boost invariant) expansion, and thermal spectra from three regions of temperature at different times in each rapidity slice. The π^0 spectrum is taken from PHENIX data. The rapidity distribution is known from the PHOBOS measurement, however, in the STAR range ($\eta = \pm 1.0$) it is effectively constant. An analysis procedure for the calorimeter has been devised which takes into account both the effects of isolation cuts and the effects of unavoidable unrecognized overlaps of background photons.

It has been found that STAR will be able to measure the yields and HBT parameters of direct photons for $p_T \leq 600$ MeV/c with about 40 million events. Fig. 31 shows the simulated results for three, one dimensional correlation functions. Q_{inv} is the usual invariant four-momentum difference, Q_{osl} is the four-momentum difference in the usual out-side-long Bertsch-Pratt system [163], and Q_{xyz} is the four-momentum difference in the x,y,z Cartesian system. The figure shows that despite the very low values of λ quite good signals (and fits) can be obtained. The individual out, side, and long radii are functions of the k_T of the photons and will be described in detail in a forthcoming paper [161]. It is currently being explored how many events would be needed to observe direct photon correlations for p_T between 1.0 and 2.0 GeV/c, but clearly it would involve much larger data samples. An interesting possibility is to use the high E_T trigger to access the region of higher p_T since it would measure the system size at a different time [162].

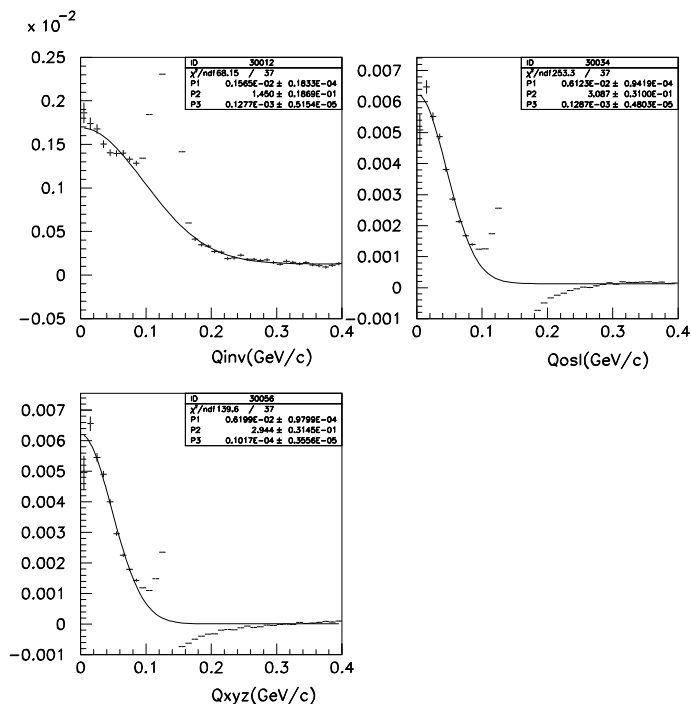


Figure 31. Correlation functions “measured” with 40 million events with full background simulation as described in the text. Top left: Q_{inv} , top right: Q_{osl} , bottom left: Q_{xyz} .

4.2.2. Spectral Distributions of the a_1 Meson

An experimental measurement of the isovector-axialvector (a_1) spectral function is highly desirable due to its important role in the search for chiral symmetry restoration in connection with measurements of thermal low-mass dileptons (which are dominated by the ρ meson (isovector-vector correlator), the chiral partner of the a_1), cf. Sec. 2.7. In Ref. [113] it has been suggested to attempt such a measurement via $\pi^\pm\gamma$ invariant-mass spectra. Calculations of photons from a_1 decays have thus far concentrated on the corresponding inclusive photon yield, which makes it very difficult to isolate the a_1 contribution and gives little information about the spectral shape of the a_1 . This is the main motivation for trying to measure the associated (charged) pion, which, however, implies strong final-state interactions including absorption. Therefore, the in-medium spectral information will primarily pertain to the more dilute stages of a heavy-ion reaction. However, the a_1 may undergo significant modifications even at moderate temperatures and densities [164]. Such effects have possibly been seen for the $\rho^0 \rightarrow \pi^+\pi^-$ [165] decay, which is “penalized” by two pion-absorption factors. Together with the dilepton measurements of the ρ meson important information on chiral symmetry restoration may be obtained.

We here report on studies [166] of the $a_1 \rightarrow \gamma\pi$ channel using transport model simulations, i.e., minimum bias $Au+Au$ UrQMD events [167] at $\sqrt{s_{NN}} = 200$ GeV. In UrQMD, $a_1 \rightarrow \gamma\pi$ has been introduced with branching ratio $BR = 0.1$, $a_1 \rightarrow \rho\pi$ $BR = 0.9$, $M_{a_1} = 1230$ MeV, and $\Gamma_{a_1}^{tot} = 400$ MeV. Only 5% of the produced a_1 ’s are found not to be absorbed in the medium, out of which 80% are from the $\gamma\pi$ channel and 20% from the

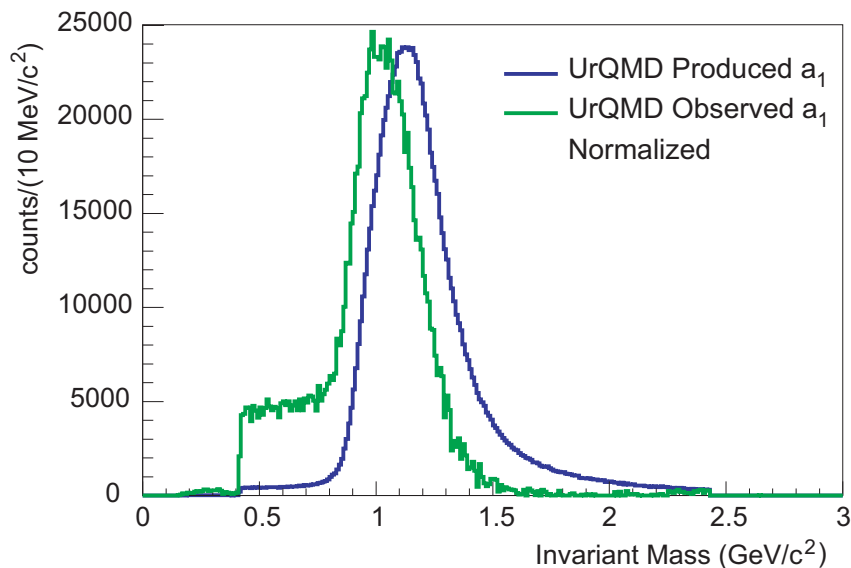


Figure 32. The spectral shape of the produced $a_1 \rightarrow \gamma\pi$ (blue line) compared to the spectral shape of $a_1 \rightarrow \gamma\pi$ that are not absorbed in the medium (green line), normalized to the number of produced a_1 .

$\rho\pi$ channel. The spectral shape of the $a_1 \rightarrow \gamma\pi$ that are not absorbed (green line in Fig. 32) is significantly different from the spectral shape of the produced a_1 's (blue line in Fig. 32), with the position of the peak shifted by about -200 MeV. Thus, the extraction of medium effects seems feasible but requires a good understanding of final-state absorption effects.

At RHIC-II, the $a_1 \rightarrow \gamma\pi$ decay can be measured using the STAR full coverage TOF. In STAR, the efficiency of measuring a γ through its conversion ($\gamma \rightarrow e^+e^-$) is 5% [168]. Therefore, 55M minimum bias $Au+Au$ collisions are necessary to measure a 3σ signal (where Hijing was used to estimate the background). In the case of the Shashlyk Calorimeter that measures low-momentum γ and could be used in STAR, the efficiency of measuring the a_1 would improve by a factor of 10.

4.3. High Statistics and Energy/Species Scan

The RHIC-II project calls for a 10-fold increase in the luminosity as currently provided by RHIC, which is very much needed for the full exploration of rare as well as (very) high- p_T signals that are currently statistics-limited. Examples include (but are not limited to) a detailed spectroscopy of heavy quarkonia, more precise values and p_T -evolution of photon and hadron R_{AA} at very high p_T , or photon flow and photon HBT at high p_T . Even with the current luminosity (which is already ~ 4 times above design), it takes 3-5 years to collect sufficient statistics for these measurements with just one species and one energy setting - clearly insufficient to explore some of the key questions about sQGP at depth and in a timely fashion.

There are, however, additional aspects and possibly missed opportunities. The above

measurements investigate the *properties* of sQGP above the critical temperature - a much needed task. But as we have emphasized in the Introduction, while the *existence* of a new state of matter has been reasonably well established at RHIC, key features of the (phase) *transition* itself (including variations across the T - μ_B phase diagram) have not been mapped out yet. The only way to do this it is via a detailed energy/species scan which in turn is possible on a reasonable timescale only with RHIC-II luminosities.

At current RHIC luminosities, even with the accelerator running for ~ 22 -28 weeks, the practical limit is at most two species per run period (year) or three energies: the dominant part of the run is spent on actual collisions and data taking. Since exploring the phase transition is mostly done with bulk observables and dileptons it does not require large statistics at any particular energy/species setting; in fact, with the luminosity upgrade at most settings sufficient amount of data could be collected in about a week.

The baryon chemical potential μ_B can be varied by changing $\sqrt{s_{NN}}$ - an operation RHIC has been designed for and successfully accomplished in several runs. RHIC experiments already collected data with heavy ions at $\sqrt{s_{NN}} = 22, 62, 130$ and 200 GeV, covering a few points on the $\sqrt{s_{NN}}$ interval between SPS and maximum RHIC energy. Recent studies have shown that one could possibly go as low as 5 GeV - the AGS range -, so measurements done by various experiments at AGS and SPS could be scrutinized (and some that are missing in retrospect could be done). While this may at first look like a repetition of earlier work we would like to re-emphasize the value of doing measurements in the entire energy range with *the very same apparatus*: with most systematic errors being the same, the *evolution* of physics quantities characterizing the transition can be traced to higher precision and with more reliable systematics.

Lower energies, however, come at the price of an approximately quadratic luminosity decrease with decreasing $\sqrt{s_{NN}}$. Therefore, as indicated at the end of Sec. 4.1.1, a meaningful energy-scan program for low-mass dileptons will crucially rely on the luminosity upgrade for RHIC-II; e.g., at $\sqrt{s_{NN}} = 30$ GeV, RHIC-II will increase the luminosity to the current one at maximum energy. Without upgrade, the luminosity loss of more than a factor of 40 from $\sqrt{s_{NN}}=200$ GeV to $\sqrt{s_{NN}}=30$ GeV would render an energy scan program for dileptons essentially useless: based on the discussions in Secs. 2.6, 2.7.2 and 3.1, a minimal accuracy of $\sim 20\%$ with $\sim 2\%$ mass resolution is needed to develop sufficient discriminating power between even rather distinct scenarios for in-medium modifications. Obviously, future refinements of theoretical approaches will further raise these requirements. Direct photon flow measurements up to very high p_T (at least 8-9 GeV) are needed to investigate contributions from parton fragmentation, jet-thermal interactions and Bremsstrahlung off quarks; however, current luminosities limit the measurement to ~ 5 -6 GeV (cf. Sec. 3.3). A tenfold increase in luminosity would extend the p_T -range by the necessary 2-3 GeV. Interferometry of pre-hadronic photons ($p_T > 2$ GeV [162]) with the precision deduced in Sec. 4.2.1 requires about 0.7B events which would, with current luminosities, make the measurement unfeasible for more than one system and/or energy. Also, many of the signals at intermediate invariant mass and transverse momentum, $M, p_T \sim 2$ GeV, where radiation from the (s)QGP dominates (cf. Secs. 2.4.1 and 2.5.3), are triggerable and therefore high luminosity is extremely valuable in this context as well. Temperature measurements of the plasma via photons as exemplified in Sec. 2.4.2 also hinge on interpretations in the context of a detailed energy and species scan. This, of course, includes

taking sufficient $p+p$ reference data at all energies where A+A collisions are performed, rather than relying on earlier results from other accelerators. Once again, the benefits of measuring both in the same detector are obvious: in many cases the systematic errors decrease by 40-50%.

Colliding different heavy-ion species renders possible to vary the geometry of the collision at fixed participant number, N_{part} . So far at RHIC several bulk observables have been found to scale with N_{part} , irrespective of collision geometry. Recently it has been found that even more subtle quantities like the (ϕ -integrated) nuclear modification factor, R_{AA} , is about the same in central $Cu+Cu$ collisions and in mid-peripheral $Au+Au$ collisions when N_{part} is the same. However, once azimuthal distributions are studied (instead of integrating over ϕ) significant differences emerge since the two collision geometries are quite different (spherical *vs* ellipsoidal) and those differences are crucial in understanding basic mechanisms like energy loss in the medium. Also, as we move to lighter ions the threshold has to be crossed below which thermalization (apparent in the hydrodynamical behavior of $Au+Au$ and even $Cu+Cu$) can no longer be sustained. Finding this point could be crucial in understanding the conditions needed for the phase transition to occur, and how pertinent signals cease.

We reiterate that higher luminosities can be used in two ways: (i) increasing the statistics of a particular data-set thus gaining access to rare probes; (ii) increasing the number of species (symmetric or asymmetric systems) and/or the energy settings by finer splitting of run times at RHIC since many important signals do not require *very* high statistics. The accelerator is the most flexible ever built and can be operated this way if there is a physics case to justify it.

5. SUMMARY AND CONCLUDING REMARKS

Let us summarize what we think are the most promising probes and developments in connection with future RHIC experiments:

- *Low-mass (axial-) vector-meson spectroscopy close to the chiral transition*

Precision dilepton data will provide detailed information on medium modifications of ρ , ω and ϕ mesons, and thus illuminate the question of hadronic mass (de-) generation. “Quality control” of theoretical models via independent constraints from symmetries, QCD sum rules and phenomenology is essential to limit the scope of viable axial-/vector (A/V) spectral functions. An excitation function will enable to discriminate effects of temperature and (net-) baryon density and thus systematically map out in-medium effects across a significant regime of the QCD phase diagram. Information on (the approach to) chiral symmetry should be inferred from a (novel) measurement of the axialvector spectral function via $\pi\gamma$ invariant-mass spectra, as well as through a well-defined combination of effective chiral hadronic models, chiral sum rules and finite-temperature QCD lattice computations of chiral order parameters (pion decay constant and four-quark condensates). The required theoretical tools are largely in place: chiral effective models for realistic axial-/vector spectral functions at finite temperature can be used to calculate the temperature dependence of order parameters (moments of “ V minus A ” spectral functions); unquenched IQCD evaluations of the latter should be pursued with high priority. A

convincing deconvolution of the vector correlator from the measured spectra will furthermore require reliable space-time descriptions of A-A collisions which we expect to emerge from envisaged progress in hydrodynamical simulations (and complementary transport models).

Footprints of chiral restoration are furthermore expected at dilepton masses around the a_1 mass (1-1.5 GeV), due to "chiral V - A mixing". To detect the pertinent continuum enhancement of a factor of ≤ 2 requires accurate charm and background determination providing a signal with no more than 20% total error; this can be achieved with the planned vertex detector upgrades in connection with sufficient statistics.

- *The highest temperatures of the matter formed at RHIC*

We have identified three promising regimes where electromagnetic radiation from the QGP is expected to be the dominant source: intermediate-mass dileptons ($M \simeq 1.5 - 3$ GeV), as well as photons and low-mass dileptons at intermediate transverse momentum ($q_t \simeq 1 - 3$ GeV). These measurements are to be augmented by γ - γ correlation analyses which yield complementary temperature and fireball-size information on the early stages.

- *QGP resonances*

The only direct way of testing the possibility of hadronic bound states/resonances in the sQGP experimentally is to search for a resonant dilepton signal. Due to the nature of QGP emission, the best sensitivity for the discovery of pertinent vector states is in the $M=2$ GeV mass region, which coincides with current expectations from lattice QCD and effective models. RHIC energies provide optimal conditions for this search as the initial temperatures are close to the anticipated dissolution temperatures of the bound states. As in the case for signatures of chiral mixing at lower mass (see above), an accurate determination of background and charm sources is mandatory restricting total experimental errors below the $\sim 20\%$ level. If the resonance states exist at masses below ~ 1.5 GeV, their discrimination from chiral mixing effects will be more involved, increasing the demand for accuracy and systematic centrality and excitation-function studies.

- *Detector and luminosity requirements*

To achieve the required background rejection and high-precision charm measurements, PHENIX needs a Hadron Blind Detector and vertex detector, and STAR needs a Time-of-Flight detector, Heavy Flavor Tracker and Data Acquisition System. Initial measurements of dileptons will be accomplished after these new detectors are in place. However, an energy scan with high statistics comparable to recent NA60 data requires significant luminosity upgrades.

A tabular summary is also given in Table 2.

Based on the arguments given in this document, we believe that electromagnetic probes in the context of future RHIC detector and luminosity upgrades for heavy-ion collisions in the $\sqrt{s_{NN}}=10$ -200 GeV regime, will, in a combined experimental and theoretical effort, result in decisive and unique new insights into QCD matter at high (energy-) density,

Measurement	Signal	Physics question	Open exp.	Open theory
very low $M_{e^+e^-}$	dN/p_T	direct γ	normalization	sole source?
low mass l^+l^-	int. yield	enhanced? depl.?	Dalitz rej.	HTL vs lattice
$\omega, \rho, \phi \rightarrow l^+l^-$	mass? width?	chiral rest.		M shift? melting?
jet- l^+l^- corr.	yield/r.p.	medium prop.	pp needed	E_{loss} mech.
intermed. M l^+l^-	spectral function	medium prop. bound $> T_c$?	rates	deg. of freedom QGP properties
$\phi, \rho \rightarrow h^+h^-$ vs e^+e^- decays	ratio vs syst., cent.	all vs. late stages of coll.	low e^+e^- BR	medium mod.
open charm,	yield flow	E_{loss} mech. therm. eq.	disp. vertex	cont. from b
low $p_T \gamma$	T vs g_{eff}	HRG vs QGP	π^0 bgd	flow/T ambiguity
HBT $\gamma < 1 GeV$	size, lifetime	therm. size vs t	resolution	other sources?
med. $p_T \gamma$	yield, R_{AA}	Cronin (E706)?		
jet tagged γ	assoc. yield	medium prop.	rates, species	jet conv./Bremsst.
high $p_T \gamma$ γ -jet	spectrum	pQCD, scale jet energy scale tomography, k_T	rates AA vs pp	
HBT ($> 2 GeV$)	size, lifetime	pre-equilib. R	rates	hadronic dominates?
all $p_T \gamma v_2$	sign, strength	thermal/jet rad.	rates	
$\gamma - \pi$ corr.	a_1 mass	chiral rest.		
all γ high y		CGC	forward cal.	

Table 2

Bottom-up view of electromagnetic probes: from observables via underlying physics question to the pertinent theoretical issues.

most notably with respect to mechanisms of hadronic mass generation in connection with the restoration of chiral symmetry, thermal radiation of unprecedented temperatures, microscopic properties of the sQGP and system size measurements during the early matter evolution.

Acknowledgments

We thank our colleagues J. Casalderrey-Solana, H. van Hees, B. Müller, P. Petreczky, T. Renk, J. Ruppert, K. Schweda, R. Seto, R. Vogt, and C. Woody for valuable input and discussions. We are particularly indebted to D. d’Enterria for providing us with Sec. 2.4.2 on “Direct Photons and Current RHIC Data”, to J. Jalilian-Marian for Sec. 2.8 on “Electromagnetic Signatures of the Color Glass Condensate”, to J. Sandweiss and his collaborators for providing us with Sect. 4.2.1 on “Direct Photon Correlations” of this manuscript and to P. Fachini for Sect. 4.2.2 (their write-ups have been edited by the three authors to fit style and scope of the manuscript). RR has been supported in part by a National Science Foundation CAREER Award under grant PHY-0449489. XZB has

been supported in part by a DOE Early Career Award and the Presidential Early Career Award for Scientists and Engineers.

REFERENCES

1. I. Arsene *et al.* [BRAHMS Collaboration], Nucl. Phys. A **757**, 1 (2005)
2. B.B. Back *et al.* [PHOBOS Collaboration], Nucl. Phys. A **757**, 28 (2005)
3. J. Adams *et al.* [STAR Collaboration], Nucl. Phys. A **757**, 102 (2005)
4. K. Adcox *et al.* [PHENIX Collaboration], Nucl. Phys. A **757**, 184 (2005)
5. Proc. of 18. Int. Conference on Nucleus-Nucleus Collisions (Quark Matter 2005), to be publ. in Nucl. Phys. **A**.
6. S. Damjanovic *et al.* [NA60 Collaboration], arXiv:nucl-ex/0510044.
7. R. Arnaldi *et al.* [NA60 Collaboration], Phys. Rev. Lett. **96**, 162302 (2006).
8. S.S. Adler *et al.* [PHENIX Collaboration], Phys. Rev. Lett **94**, 232301 (2005)
9. L.E. Gordon and W. Vogelsang, Phys. Rev. D **48**, 3136 (1993); Phys. Rev. D **50**, 1901 (1994);
P. Aurenche *et al.*, Phys. Lett. B **140**, 87 (1984); Nucl. Phys. B **297**, 661 (1988).
10. S. Turbide, C. Gale and R.J. Fries, Phys. Rev. Lett. **96**, 032303 (2006).
11. R. Chatterjee, E.S. Frodermann, U.W. Heinz and D.K. Srivastava, Phys. Rev. Lett. **96**, 202302 (2006).
12. F. Karsch and E. Laermann, arXiv:hep-lat/0305025.
13. P. Braun-Munzinger, K. Redlich and J. Stachel, arXiv:nucl-th/0304013.
14. M. Asakawa, T. Hatsuda and Y. Nakahara, Nucl. Phys. **A715**, 863 (2003).
15. F. Karsch, Lect. Notes Phys. **583**, 209 (2002) [arXiv:hep-lat/0106019].
16. B. Muller and K. Rajagopal, Eur. Phys. J. C **43**, 15 (2005).
17. E. V. Shuryak and I. Zahed, arXiv:hep-ph/0406100.
18. D. d'Enterria and D. Peressounko, Eur. Phys. J. C **46**, 451 (2006)
19. D. K. Srivastava and B. Sinha, Phys. Rev. C **64**, 034902 (2001); D. K. Srivastava, Pramana **57**, 235 (2001).
20. J. e. Alam, S. Sarkar, T. Hatsuda, T. K. Nayak and B. Sinha, Phys. Rev. C **63**, 021901 (2001).
21. J.e. Alam, J.K. Nayak, P. Roy, A.K. Dutt-Mazumder and B. Sinha, nucl-th/0508043.
22. F.D. Steffen and M.H. Thoma, Phys. Lett. B **510**, 98 (2001).
23. P. Huovinen, P.V. Ruuskanen and S.S. Räsänen, Phys. Lett. B **535**, 109 (2002); S.S. Räsänen, Nucl. Phys. A **715**, 717 (2003); H. Niemi, S.S. Räsänen and P.V. Ruuskanen in "CERN Yellow Report on Hard Probes in Heavy Ion Collisions at the LHC", arXiv:hep-ph/0311131.
24. M. Glück, E. Reya and A. Vogt, Phys. Rev. D **48**, 116 (1993) [Erratum-ibid. D **51** (1995) 1427].
25. H. van Hees, V. Greco and R. Rapp, Phys. Rev. C **73**, 034913 (2006).
26. L. Grandchamp, R. Rapp and G.E. Brown, Phys. Rev. Lett. **92**, 212301 (2004).
27. J. Casalderrey-Solana and E.V. Shuryak, arXiv:hep-ph/0408178.
28. R. Rapp and J. Wambach, Adv. Nucl. Phys. **25**, 1 (2000).
29. J. Alam, S. Sarkar, P. Roy, T. Hatsuda and B. Sinha, Ann. Phys. **286**, 159 (2001).
30. C. Gale and K. Haglin, in R.C. Hwa and X.-N. Wang (eds.), *Quark gluon plasma 3*

- (2003) 364 [arXiv:hep-ph/0306098].
31. M. Harada and K. Yamawaki, Phys. Rept. **381**, 1 (2003).
 32. G.E. Brown and M. Rho, Phys. Rept. **396**, 1 (2004).
 33. G. Agakichiev *et al.* [CERES Collaboration], Eur. Phys. J. C **41**, 475 (2005).
 34. R. Rapp, J. Phys. **G31**, S217 (2005).
 35. E.L. Feinberg, Nuovo Cimento A **34**, 391 (1976).
 36. L.D. McLerran and T. Toimela, Phys. Rev. D **31**, 545 (1985).
 37. M.C. Abreu *et al.* [NA50 Collaboration], Eur. Phys. J. **C14** (2000) 443.
 38. M.M. Aggarwal *et al.* [WA98 Collaboration], Phys. Rev. Lett. **85**, 3595 (2000).
 39. M.M. Aggarwal *et al.* [WA98 Collaboration], Phys. Rev. Lett. **93**, 022301 (2004).
 40. R. Rapp and J. Wambach, Eur. Phys. J. **A6**, 415 (1999).
 41. R. Rapp and E.V. Shuryak, Phys. Lett. B **473**, 13 (2000).
 42. G.E. Brown and M. Rho, Phys. Rep. **269**, 333 (1996).
 43. I. Kvasnikova, C. Gale and D.K. Srivastava Phys. Rev. C **65**, 064903 (2002).
 44. K. Gallmeister, O.P. Pavlenko and B.Kämpfer, Phys. Lett. B **473**, 20 (2000).
 45. S. Turbide, R. Rapp and C. Gale, Phys. Rev. C **69**, 014903 (2004).
 46. W. Liu and R. Rapp, arXiv:nucl-th/0604031.
 47. D. Adamova *et al.* [CERES Collaboration], Phys. Rev. Lett. **91**, 042301 (2003).
 48. F. Karsch, S. Datta, E. Laermann, P. Petreczky, S. Stickan and I. Wetzorke, Nucl. Phys. A **715**, 701 (2003).
 49. E. Braaten, R. D. Pisarski and T. C. Yuan, Phys. Rev. Lett. **64**, 2242 (1990).
 50. P. Petreczky, talk at the 2. RHIC-II meeting, Brookhaven National Laboratory, Apr 29-30, 2005.
 51. F. Arleo *et al.*, Chap. 4 of CERN Yellow Report CERN-2004-009 (Geneva, Switzerland, 2004), arXiv:hep-ph/0311131.
 52. S. Gupta, Phys. Lett. B **597**, 57 (2004).
 53. D. Fernandez-Fraile and A. Gomez-Nicola, arXiv:hep-ph/0512283.
 54. C. R. Allton *et al.*, Phys. Rev. D **71**, 054508 (2005)
 55. M. Prakash, R. Rapp, J. Wambach and I. Zahed, Phys. Rev. C **65**, 034906 (2002).
 56. M. A. Shifman, A. I. Vainshtein and V. I. Zakharov, Nucl. Phys. B **147**, 385 (1979).
 57. M. Asakawa and C.M. Ko, Nucl. Phys. A **560**, 399 (1993).
 58. F. Klingl, N. Kaiser and W. Weise, Nucl. Phys. A **624**, 527 (1997).
 59. S. Leupold, W. Peters and U. Mosel, Nucl. Phys. A **628**, 311 (1998)
 60. J. Ruppert, T. Renk and B. Muller, Phys. Rev. C **73**, 034907 (2006).
 61. S. Weinberg, Phys. Rev. Lett. **18**, 507 (1967).
 62. T. Das, V. S. Mathur and S. Okubo, Phys. Rev. Lett. **19**, 859 (1967).
 63. E.G. Floratos, S. Narison and E. de Rafael, Nucl. Phys. **B155**, 115 (1979).
 64. S. Narison, Z. Phys. **C14**, 263 (1982).
 65. V. Dmitrasinovic, Phys. Rev. D **57**, 7019 (1998).
 66. J. I. Kapusta and E. V. Shuryak, Phys. Rev. D **49**, 4694 (1994).
 67. R. Rapp, Phys. Rev. C **63**, 054907 (2001).
 68. P. Arnold, G. D. Moore and L. G. Yaffe, JHEP **0112**, 009 (2001).
 69. R. Rapp, arXiv:nucl-th/0204003.
 70. S. Bathe [PHENIX Collaboration], Proc. of 18. Int. Conference on Nucleus-Nucleus Collisions (Quark Matter 2005), to be publ. in Nucl. Phys. **A** [arXiv:nucl-ex/0511042].

71. M. Gyulassy, I. Vitev, X. N. Wang and B. W. Zhang, arXiv:nucl-th/0302077.
72. F. Gelis, K. Kajantie and T. Lappi, Phys. Rev. Lett. **96**, 032304 (2006).
73. E.V. Shuryak and L. Xiong, Phys. Rev. Lett. **70**, 2241 (1993).
74. M. Strickland, Phys. Lett. B **331**, 245 (1994).
75. B. Kampfer, O.P. Pavlenko, A. Peshier and G. Soff, Phys. Rev. C **52**, 2704 (1995).
76. D.K. Srivastava, M.G. Mustafa and B. Muller, Phys. Rev. C **56**, 1064 (1997).
77. K.J. Eskola, B. Muller and X.N. Wang, Phys. Lett. **B374**, 20 (1996).
78. D.M. Elliott and D.H. Rischke, Nucl. Phys. **A671**, 583 (2000).
79. F. Gelis, H. Niemi, P.V. Ruuskanen and S.S. Räsänen, J. Phys. G **30**, S1031 (2004)
80. S.A. Bass, B. Müller and D.K. Srivastava, Phys. Rev. Lett. **90**, 082301 (2003)
81. T. Renk, S.A. Bass and D.K. Srivastava, Phys. Lett. B **632**, 632 (2006).
82. T. Renk, arXiv:hep-ph/0408218.
83. D. K. Srivastava, Phys. Rev. C **71**, 034905 (2005).
84. T. Sakaguchi [PHENIX Collaboration], arXiv:nucl-ex/0504013.
85. S. Turbide, C. Gale, S. Jeon and G.D. Moore, Phys. Rev. C **72**, 014906 (2005).
86. D. Turbide, C. Gale, D.K. Srivastava and R. Fries, arXiv:hep-ph/0601042.
87. R. Rapp, M. Urban, M. Buballa and J. Wambach, Phys. Lett. **B417**, 1 (1998).
88. J.V. Steele, H. Yamagishi and I. Zahed, Phys. Rev. D **56**, 5605 (1997).
89. R. Rapp, G. Chanfray and J. Wambach, Nucl. Phys. **A617**, 472 (1997).
90. M. Post, S. Leupold and U. Mosel, Nucl. Phys. **A689**, 753 (2001).
91. M.F.M. Lutz, G. Wolf and B. Friman, Nucl. Phys **A706**, 431 (2002)
92. D. Cabrera, E. Oset and M.J. Vicente-Vacas, Nucl. Phys. **A705** (2002) 90.
93. V.L. Eletsky, M. Belkacem, P.J. Ellis and J.I. Kapusta, Phys. Rev. C **64**, 035202 (2001).
94. T. Ishikawa *et al.*, Phys. Lett. **B608**, 215 (2005).
95. R. Muto *et al.*, arXiv:nucl-ex/0511019.
96. D.N. Voskresensky, Nucl. Phys. **A744**, 378 (2004).
97. R. Rapp, Nucl. Phys. **A661**, 33 (1999).
98. J.V. Steele and I. Zahed, Phys. Rev. D **60**, 037502 (1999).
99. G.E. Brown and M. Rho, Phys. Rev. Lett. **66**, 2720 (1991); Phys. Rept. **269**, 333 (1996)
100. M. Harada and C. Sasaki, Phys. Rev. D **73**, 036001 (2006).
101. Y. Hidaka, O. Morimatsu and M. Ohtani, Phys. Rev. D **73**, 036004 (2006).
102. M. Velkovsky and E.V. Shuryak, Phys. Rev. D **56**, 2766 (1997).
103. E.V. Shuryak and I. Zahed, Phys. Rev. C **70**, 021901 (2004)
104. G.E. Brown, C.H. Lee, M. Rho and E.V. Shuryak, Nucl. Phys. **A740**, 171 (2004).
105. M. Mannarelli and R. Rapp, Phys. Rev. C **72**, 064905 (2005).
106. M. Dey, V.L. Eletsky and B.L. Ioffe, Phys. Lett. **B252**, 620 (1990).
107. H. van Hees and R. Rapp, Phys. Rev. Lett., in press (2006) [arXiv:hep-ph/0603084].
108. H. van Hees and R. Rapp, arXiv:hep-ph/0604269.
109. K. Dusling, D. Teaney and I. Zahed, arXiv:nucl-th/0604071.
110. T. Renk and J. Ruppert, arXiv:hep-ph/0605130.
111. F. Riek, H. van Hees and J. Knoll, arXiv:nucl-th/0607023.
112. S. Damjanovic (2005), private communication.
113. R. Rapp, Nucl. Phys. A **725**, 254 (2003).

- 114.J. Adams *et al.* [STAR Collaboration], Phys. Rev. Lett. **92**, 092301 (2004).
- 115.P. Fachini, J. Phys. G **30**, S735 (2004).
- 116.E.V. Shuryak and G.E. Brown, Nucl. Phys. A **717**, 322 (2003).
- 117.W. Broniowski, W. Florkowski and B. Hiller, Phys. Rev. C **68**, 034911 (2003).
- 118.S. Pratt and W. Bauer, Phys. Rev. C **68**, 064905 (2003).
- 119.R. Rapp, Phys. Rev. C **66**, 017901 (2002).
- 120.R. Barate *et al.* [ALEPH Collaboration], Eur. Phys. J. C **4**, 409 (1998).
- 121.R. Rapp, *Pramana* **60**, 675 (2003) [arXiv: hep-ph/0201101].
- 122.T. Hirano and M. Gyulassy, Nucl. Phys. A **769**, 71 (2006).
- 123.S.A. Bass and A. Dumitru, Phys. Rev. C **61**, 064909 (2000).
- 124.D. Teaney, J. Lauret and E.V. Shuryak, Phys. Rev. Lett. **86**, 4783 (2000).
- 125.Z.W. Lin, C.M. Ko, B.A. Li, B. Zhang and S. Pal, Phys. Rev. C **72**, 064901 (2005).
- 126.W. Cassing and S. Juchem, Nucl. Phys. **A672**, 417 (2000).
- 127.P. Huovinen and M. Prakash, Phys. Lett. **B450**, 15 (1999).
- 128.W. Cassing, E.L. Bratkovskaya, R. Rapp and J. Wambach, Phys. Rev. C **57**, 916 (1997)
- 129.T. Renk, R. Schneider, and W. Weise, Phys. Rev. C **66**, 014902 (2002).
- 130.E. Iancu and R. Venugopalan, arXiv:hep-ph/0303204;
J. Jalilian-Marian and Y.V. Kovchegov, Prog. Part. Nucl. Phys. **56**, 104 (2006)
- 131.F. Gelis and J. Jalilian-Marian, Phys. Rev. D **66**, 014021 (2002); Phys. Rev. D **66**, 094014 (2002); Phys. Rev. D **67**, 074019 (2003).
- 132.B.Z. Kopeliovich, J. Raufeisen, A.V. Tarasov and M.B. Johnson, Phys. Rev. C **67**, 014903 (2003);
M.B. Johnson *et al.*, Phys. Rev. C **65**, 025203 (2002).
- 133.R. Baier, A.H. Mueller and D. Schiff, Nucl. Phys. A **741**, 358 (2004);
M.A. Betemps and M.B. Gay Ducati, Phys. Rev. D **70**, 116005 (2004).
- 134.J. Jalilian-Marian, Nucl. Phys. A **739**, 319 (2004); Nucl. Phys. A **753**, 307 (2005);
arXiv:hep-ph/0509338.
- 135.A. Dumitru, A. Hayashigaki and J. Jalilian-Marian, Nucl. Phys. A **765**, 464 (2006).
- 136.R.D. Pisarski, Phys. Lett. **100B** (1982) 155
- 137.D. Miskowiec *et al.* [CERES Collaboration], arXiv:nucl-ex/0511010.
- 138.L. Holt and K. Haglin, J. Phys. G **31**, S245 (1995);
S. Pal, C.M. Ko and Z. Lin, Nucl. Phys. A **707**, 525 (2002);
L. Alvarez-Ruso, V. Koch, Phys. Rev. C **65**, 054901 (2002).
- 139.A. Kozlov *et al.* [PHENIX Collaboration], Proc. of 18. Int. Conference on Nucleus-Nucleus Collisions (Quark Matter 2005), to be publ. in Nucl. Phys. **A** [arXiv:nucl-ex/0510016].
- 140.X. Cai, *et al.* [STAR Collaboration], Proc. of 18. Int. Conference on Nucleus-Nucleus Collisions (Quark Matter 2005), to be publ. in Nucl. Phys. **A** [arXiv:nucl-ex/0511004];
J. Adams *et al.* [STAR Collaboration], Phys. Lett. B **612**, 181 (2005).
- 141.J. Rafelski, J. Letessier, G. Torrieri, Phys. Rev. C **72**, 024905 (2005).
- 142.D. Adamova *et al.* [CERES Collaboration], Phys. Rev. Lett. **96**, 152301 (2006)
- 143.E. Scomparin *et al.* (NA60 Collaboration), Proc. of 18. Int. Conference on Nucleus-Nucleus Collisions (Quark Matter 2005), to be publ. in Nucl. Phys. **A**.
- 144.S.S. Adler *et al.* [PHENIX Collaboration], Phys. Rev. Lett. **96**, 032302 (2006).

- 145.S.S. Adler *et al.* [PHENIX Collaboration], *Phys. Rev. Lett.* **96**, 032301 (2006).
- 146.N. Armesto, S. Dainese, C. Salgado, and U. Wiedemann, *Phys. Rev. D* **71**, 054027 (2005).
- 147.M. Djordjevic, M. Gyulassy, R. Vogt and S. Wicks, *Phys. Lett. B* **632**, 81 (2006).
- 148.S.S. Adler *et al.* [PHENIX Collaboration], *Phys. Rev. Lett.* **94**, 082301 (2005).
- 149.S.S. Adler *et al.* [PHENIX Collaboration], *Phys. Rev. C* **72**, 024901 (2005).
- 150.H. van Hees and R. Rapp, *Phys. Rev. C* **71**, 034907 (2005).
- 151.G.D. Moore and D. Teaney, *Phys. Rev. C* **71**, 064904 (2005).
- 152.S.S. Adler *et al.* [PHENIX Collaboration], *Phys. Rev. Lett.* **96**, 032301 (2006).
- 153.B.I. Abelev *et al.* [STAR Collaboration], arXiv:nucl-ex/0607012.
- 154.S.S. Adler *et al.* [PHENIX Collaboration], *Phys. Rev. C* **72**, 024901 (2005); S. Sakai, arXiv:nucl-ex/0510027.
- 155.N.M. Kroll and W. Wada, *Phys. Rev.* **98**, 1355 (1955).
- 156.M. Shao *et al.* *Nucl. Instrum. Meth. A* **558** 419 (2006).
- 157.Z. Xu *et al.* LBNL-PUB-5509, “A heavy flavor tracker for STAR”, <http://www-library.lbl.gov/docs/PUB/5509/PDF/PUB-5509.pdf>;
K. Schweda *et al.*, Proc. of 18. Int. Conference on Nucleus-Nucleus Collisions (Quark Matter 2005), arXiv:nucl-ex/0510003.
- 158.Z. Frankel *et al.*, *Nucl. Instrum. Meth. A* **546**, 466 (2005).
- 159.H. Satz, arXiv:hep-ph/0512217.
- 160.R. Rapp, D. Cabrera and H. van Hees, arXiv:nucl-th/0608033.
- 161.J. Sandweiss *et al.*, in preparation.
- 162.S.A. Bass, B. Müller and D.K. Srivastava, *Phys. Rev. Lett.* **93**, 162301 (2004).
- 163.G. Bertsch and S. Pratt, *Phys. Rev. Lett.* xxx
- 164.R. Rapp, *Eur. Phys. J. A* **18**, 459 (2003).
- 165.J. Adams *et al.* [STAR Collaboration], *Phys. Rev. Lett.* **92**, 092301 (2004).
- 166.P. Fachini, private communication (2006).
- 167.S. Vogel and M. Bleicher, arXiv:hep-ph/0607242.
- 168.J. Adams *et al.* [STAR Collaboration], *Phys. Rev. C* **70**, 044902 (2004).